Archives of Civil and Mechanical Engineering (2024) 24:148
https://doi.org/10.1007/s43452-024-00958-x

ORIGINAL ARTICLE

Phase transformation effect on residual stress development in fusion welding of dissimilar stainless steels with different thickness

Swagat Dwibedi[1] · Bikash Kumar[2] · Swarup Bag[1]

Received: 6 October 2023 / Revised: 13 January 2024 / Accepted: 21 April 2024 / Published online: 14 May 2024

Abstract
The residual stress creates deleterious effects on joint properties of dissimilar welding due to differential thermophysical properties and mechanical constraints of dissimilar thickness. Accounting of solid-state phase transformation (SSPT) through the understanding of solidification behavior enhances the prediction accuracy of residual stress. The characterization of microstructural features improves the fundamental understanding of the residual stress evaluation. An attempt is made to comprehend the dependence of heat input on phase transformation and its effect on the generation of compressive residual stress in dissimilar welding. Three distinct heat inputs of 52, 63, and 77 J/mm are considered in micro-plasma arc welding (μ-PAW) of SS316L and SS310 with thicknesses of 800 μm and 600 μm, respectively. The measurement of residual stress is performed using the X-ray diffraction (XRD) method. The variation of $\delta_{ferrite}$ from 11.2 to 7.9% is analogous to the variation of average $\delta_{ferrite}$ lath size from 412 to 1040 nm, where inter-dendritic spacing varies from ~ 10 μm to ~ 20 μm. The solidification mode is identified as ferritic-austenitic (FA), which results in the formation of skeletal and lathy $\delta_{ferrite}$ structures. Electron Backscatter Diffraction (EBSD) results show an increase in heat input leads to an increase in low-angle grain boundaries that results in a rise in the residual stress value. The phase fraction and residual stresses are computed employing a finite element (FE) based thermal-metallurgical-mechanical (TMM) model including the effect of SSPT. The reasonable agreement between the computed and experimental measurements with a maximum error of ~ 8.5% in weld size, ~ 7.5% in peak temperature, ~ 16% in retained $\delta_{ferrite}$, ~ 17% in residual stress, and ~ 5% in distortion demonstrates the reliability of the developed model. A lower level of heat input (52 J/mm) allows the formation of a high amount of $\delta_{ferrite}$, which generates comparatively more compressive stress as a disparity in thermal expansion coefficient $\alpha_{Ni} \sim 1.6\alpha_{Cr}$ aids in the reduction of residual stress.

Keywords Finite element modelling · Solidification mode · Phase fraction · Grain misorientation · Residual stress · Distortion

1 Introduction

Joining dissimilar grades of austenitic stainless steel (ASS) has found widespread application in the field of automobile, aerospace, medical, and power generation industries and pressurized water reactors [1, 2]. In particular, the SS300 series offers enhanced corrosion resistance and cryogenic properties due to the presence of high chromium and nickel percentages [3]. Dissimilar ASS joints are primarily recognized for their superior corrosion-resistant behavior, better strength at elevated temperatures, and excellent low-temperature fatigue properties. However, with low specific heat and thermal conductivity, high thermal expansion coefficients of ASS often exhibit inferior mechanical properties of welded joints owing to (a) the development of high residual stresses and structural deformation propensity and (b) ignorance of the role of microstructural attribute in residual stress evolution [4]. The accurate prediction of residual stress is always of great interest as it paves the road to eliminate or mitigate it.

The flexibility in power distribution to produce concentrated arc, μ-PAW is a potential candidate for welding

✉ Swarup Bag
swarupbag@iitg.ac.in

[1] Department of Mechanical Engineering, Indian Institute of Technology Guwahati, Guwahati, Assam 781039, India

[2] Department of Industrial and Production Engineering, Dr. B. R. Ambedkar National Institute of Technology Jalandhar, Jalandhar, Punjab 144008, India

dissimilar joints. However, the problem of residual stress arises from the non-uniform heat flux distribution, and it becomes more complex when the welded components have different coefficients of thermal expansion, thermal conductivity, severe variation in composition change, and different microstructures [5, 6]. Several researchers have made an effort to understand the mechanism for the development and mitigation of residual stresses in dissimilar welded joints [7–9]. Dawes [10] opined that because the grades of ASS expand 50% more than carbon steels and have poorer heat conductivity, they are more likely to bend and expand unevenly when combined. Usually, high magnitude of residual stress is localized in the heat-affected zone (HAZ) due to phase-change-induced expansion during cooling [11]. Akbari and Sattari-Far [12] showed that heat input mainly controls the level of residual stress in multipass dissimilar welding between stainless steel and carbon steel. The compressive stress in the stainless steel side reduces with a decrease in heat input. However, tensile stress in the stainless steel side reduces with a decrease in heat input. Maurya et al [13] depicted that excessive heat input caused residual stress to rise by 16 and 19%, respectively, in the longitudinal and transverse directions for dissimilar welding of Inconel and stainless steel. In all these cases, the effect of phase transformation was neglected.

The influence of heat input on microstructural evolution and phase transformation effect for similar and dissimilar ASS joints are well studied in the literature. Hsieh et al [14] studied the precipitation and strengthening behavior of dissimilar ASS joints and identified higher hardness values due to Cr-rich massive $\delta_{ferrite}$ at solidified metal. The grain refinement of $\delta_{ferrite}$ is enriched upon increasing the number of weld passes for dissimilar ASS joints [15]. Kianersi et al [16] observed three different morphologies of $\delta_{ferrite}$ (skeletal, acicular, and lathy) in laser-welded ASS structures. The non-equilibrium phases evolved here due to the rapid cooling of welding processes. Relatively higher heat input or lower cooling rate exhibits coarsening of the ferritic-dendritic core and widening of inter-dendritic spacing, which resulted in dampening of tensile strength of welded joints. Harjo et al [17] reported that the compressive strain was generated in the ferrite phase, whereas the tensile strain appeared in the $\gamma_{austenite}$ matrix. Further, Thibault et al [18] observed compressive residual stress in the weld joint due to lowered martensitic transformation temperature of 13%Cr-4%Ni steel alloy. Hsieh et al [19] examined the propensity of tensile residual stress enhanced with enrichment of $\delta_{ferrite}$ content of SS304. A feathery ferrite and compressive stress pattern are observed by Chen et al [20] in the hybrid laser-welding of ASS. However, the mechanism behind the development of stress was not elucidated adequately.

The chemical composition, cooling rate, and primary solidification mode rendered during welding are the main factors influencing the formation of $\delta_{ferrite}$. It is realized that the amount and distribution of $\delta_{ferrite}$ in an ASS weldment is crucial since it determines the thermal stability, mechanical performance, and residual stress generation of the weld joint. The primary reason for the generation of residual stresses is linked with the solidification of the weld since the dilution occurs during liquid-to-solid phase transformation, and the solid-state phase transformation (SSPT) occurs after solidification with a differential cooling rate [21]. It is well known that residual stress tops the list in causing severe damage to a welded specimen [22–24]. Therefore, predicting, controlling, and finding ways to reduce stress developed in a welded structure remains the utmost priority.

Researchers have tried to predict residual stresses using experimental measurements aided by numerical models [25, 26]. Deng [27] showed the importance of martensitic transformation in the stress generated in medium carbon steel. The variation in the longitudinal stress value was minimized by considering the SSPT effect. Several researchers closely resembled the predicted value with the experimental results by incorporating SSPT [28–30]. Zubairuddin et al [28] reported drastic variation in predicting the value of transverse stress with (542 MPa) and without (635 MPa) consideration of the phase transformation effect in the 9Cr-1Mo steel joint. The authors suggested that austenite to martensite transformation accounts for a significant difference in the stress value. Hamelin et al [29] reported that high welding speed resulted in more martensite because of the high cooling rate. Even the prediction of residual stresses resembled the experimental data when phase transformation plasticity was implemented in the numerical model. Yaghi et al [30] reported a stress reversal from tensile to compressive in the fusion zone by including the effect of SSPT and TRIP in the case of P91 steel. Li et al [31] observed that consideration of SSPT accurately predicts the residual stress in dissimilar P22-SS304 joints. Kumar and Bag [32] predicted a low value (810 MPa) of longitudinal stress considering the phase transformation effect and minimum residual stress are observed under the least heat input (45 J/mm) characterized by high $\delta_{ferrite}$ content, finer lath size, and lower inter-dendritic spacing [33]. Taraphdar et al [34] indicated that incorporating the SSPT effect provided significantly better correspondence with the measured value for longitudinal (~ 205 MPa) and transverse (~ 230 MPa) stress fields in the case of carbon steel. A similar observation is reported by Kubiak and Piekarska [35]. Mi et al [36] indicated that physical properties, volume change, and transformation-induced plastic strain are highly influential for reliable estimation of residual stress. Accounting both diffusive and displacive transformations in a TMM improves the welding distortion pattern. In fusion welding of ultra-high strengthened carbon steel, the microstructure consisting of bainite with a lower proportion of martensite also influences the residual stress evolution [37]. Considering the microstructural phenomena details and their kinetics during solidification improves the reliability of residual stress calculation.

The measurement of residual stress is one of the daunting tasks following any destructive and non-destructive techniques. Several researchers have developed contemporary novel techniques to enhance the accuracy of measurement of residual stress components [38–40]. Shen et al [38] determined surface residual stress based on spherical indentation. The localization of the largest pile-up around an indentation indicates the maximum residual stress. The particular link between pile-up after unloading and biaxial stress allows us to accurately detect the components of residual stress. Taraphdar et al [39] developed a flexible deep hole contour technique that does not need a complete section of the specimen and has the potential to measure through-thickness residual stress patterns with a relatively lower degree of damage of tested samples. Additionally, Elata et al [40] developed the residual stress measurement method following the electromechanical bifurcation response of a clamped–clamped beam. The presence of weld grooves significantly impacts on residual stress generation [41]. By accommodating the unequal V-groove pattern, the magnitude of residual stress components can be minimized near the root of the weld joint. An alternating weld pass sequence also dampens residual stress generation. However, the application of a single-directional weld pass sequence in an equal double-V groove configuration leads to the agglomeration of higher tensile residual stress [42]. Literature indicates that maintaining an optimum level of heat input governs the quality of weld joints and the presence of tensile residual stress tends to affect the fatigue strength of a weld joint. Thus, the likelihood of generating compressive stresses in the welded structure by considering the influence of microstructural transformation improves the joint quality [43, 44]. The summary of significant advancement in residual stress development in the fusion welding process is presented in Table 1.

It is obvious from the literature that thermal stability, mechanical features, and residual stress of dissimilar ASS welding are controlled by the distribution and quantity of $\delta_{ferrite}$ at the fusion zone. Further, the estimation of residual stress in dissimilar austenitic steels is highly complicated where the solidification behavior and morphology are predominant. There is a significant lack of substantial work on dissimilar joints with the incorporation of SSPT is yet to be explored. Hence, the objective of the present study is to investigate the mitigation of residual stress by controlling microstructural morphologies that can elude the failures of a welded joint. Therefore, an attempt is made to understand the solidification behavior of the weld metal as well as its correlation with microstructural features and residual stress distribution. A sequentially coupled thermal-metallurgical-mechanical model (TMM) is developed and implemented using an in-house developed code through the subroutine of available commercial software. Further, numerically obtained residual stress values are validated with the experimentally measured data. The role of microstructure developed in dissimilar welding on residual stress generation is also established in the present work. An attempt is made to understand the dependence of cooling rate on phase transformation and its effect on the generation of compressive residual stress in dissimilar welding.

2 Experimental methodology

Thin steel sheets (SS316L and SS310) are autogenously joined using the µ-PAW process with 800 µm and 600 µm thicknesses, respectively. This welding process provides excellent joint characteristics at a relatively lower cost than laser and electron beam welding processes [45]. The elemental composition (Table 2) of the base metals SS316L and SS310 primarily comprises Cr and Ni with the inclusion of minor alloying elements (Si, Mn, Mo), and the rest Fe. The complete experimental setup and the feasible range of experimental data are presented elsewhere [46]. Figure 1a–d presents the process window for dissimilar weld joints. The different combinations of current (8–15 A) and speed (2.15–4.65 mm/s) lead to any of the following three weld conditions: (i) insufficient heating leads to no melting/no fusion, (ii) optimum/sufficient heat input corresponds to the formation of uniform weld bead with no visual imperfections, and (iii) overheating leads to burn through of the joints. The feasible het input range is identified as 52–77 J/mm, in which dissimilar joints produced are free from any visual imperfections such as undercut, cracking, underfill, and sagging. The plasma and shielding gas flow rates are 0.7 L/s and 7 L/s, respectively. The nozzle and electrode diameters used are 1.2 mm and 1.0 mm, respectively.

In the current examination, the effect of phase transformation on residual stresses is examined experimentally and numerically. From the feasible range, three parameters, 52 J/mm (L_{52}), 63 J/mm (M_{63}), and 77 J/mm (H_{77}), are selected as the criteria of low, medium, and high heat input context. Further, samples extracted from the dissimilar joints are subjected to microscopic, elemental, electron backscatter diffraction (EBSD), and X-ray diffraction (XRD) analysis. Also, a coordinate measuring machine (CMM) is used to measure the longitudinal and out of the plane distortion for the dissimilar joints. The microscopic analysis is done using a field emission scanning electron microscope (FESEM) to identify the presence of lathy/skeletal ferrite in the austenitic matrix. The relative amount of $\delta_{ferrite}$ in the austenite matrix is calculated. The elemental analysis helps to get an idea regarding the resulting composition of the different regions of the FZ, which aids in determining the concept of solidification mode by calculation of $Cr_{eq.}/Ni_{eq.}$ ratio using the Schaeffler diagram. Also, $Cr_{eq.}$ and $Ni_{eq.}$ is marked on the Fe–Ni-Cr ternary diagram (70 wt.

Table 1 Summary of research progress on residual stress development in the fusion welding process

Authors [Reference]	Material(s)	Process	Process parameters	Remarks on the development and measurement of residual stresses
Anawa and Olabi [7]	SS316L-LCS	LBW	(1.05–1.43) kW, (500–1000) mm/min	The value measured by the hole drilling method shows a decrease (330 MPa⟶142 MPa) in residual stress value with increasing speed (500 mm/min⟶1000 mm/min)
Kumar et al. [8]	Inconel 617	GTAW, HW-GTAW	(1.19–1.58) kJ/mm, (0.75–1) kJ/mm	HW-GTAW measures 20% (180–200 MPa) of the fusion zone to be under tensile stress (measured by the DHD method) as compared to 70% (205–218 MPa) in conventional GTAW
Akbari and Sattari-Far [12]	Carbon steel-SS304	GTAW, SMAW,	(95–145) A, (9–28) V, (0.55–4.1) mm/s	In dissimilar joints, the value of peak stresses (tensile or compressive) (measured by the HD method) exits in the SS component due to the higher value of yield strength of SS as compared to carbon steel, and the value of residual stress decreases with increase in heat input (h) (h⟶250 MPa, 0.8 h⟶210 MPa, 0.5 h⟶160 MPa)
Maurya et al. [13]	sDSS 2507- Inconel 625	GTAW	(0.73, 1.4) kJ/mm	Excessive heat input results in an increase in the value of residual stress (measured by the DHD method) by 16%, 19% in the longitudinal (423 MPa⟶0.73 kJ/mm, 491 MPa⟶1.4) kJ/mm) and transverse directions (198 MPa⟶0.73 kJ/mm, 235 MPa⟶1.4) kJ/mm)
Thibault et al. [18]	13%Cr–4%Ni SS	GMAW	(1.9–2.5) kJ/mm	Compressive residual stress (measured by ND technique) is reported in the joint due to lowered martensitic transformation temperature. Also, as a result of PWHT, tensile and compressive stress values reduced from 534⟶136 MPa and 371⟶152 MPa, respectively
Zubairuddin et al. [28]	9Cr-1Mo steel	GTAW	90 A, 100 mm/min	The value of residual stress (measured with XRD) is obtained as 560 MPa, and the predicted stress value is reported as 542 MPa (with P_{trans}) and 635 MPa (without P_{trans}). The difference in predicted value is due to austenite to martensite transformation

Table 1 (continued)

Authors [Reference]	Material(s)	Process	Process parameters	Remarks on the development and measurement of residual stresses
Kumar et al. [33]	SS304	LBW	(45, 56, 75) J/mm	Minimum stress (measured by XRD) value is obtained under the least heat input (45 J/mm) condition and is characterized by high $\delta_{ferrite}$ content, finer lath size, and lower inter-dendritic spacing
Taraphdar et al. [41]	HSLA steel	SMAW	100–140 A, 22–26 V, 30–50 cm/min	A reduction of 12% in the magnitude of S11 is reported (measured by DHD) near the bottom of the weld joint by the use of an unequal-V groove (331 MPa) weld as compared to an equal-V groove (378 MPa)
Taraphdar et al. [42]	SA516 Gr.70- SS304L	GMAW	168–248 A, 24–27 V, (26, 80) cm/min	Application of narrow grove geometry resulted in a reduction in the measured (by DHD) value of residual stress (S11) from 202 to 173 MPa at a distance of 1 mm from the top of the weld surface

Abbreviation: LBW⟶ laser beam welding, GTAW⟶ gas tungsten arc welding, GMAW⟶ gas metal arc welding, HW-GTAW⟶ hot-wire gas tungsten arc welding, HD⟶ deep hole drilling, DHD⟶ deep hole drilling, ND⟶ neutron diffraction, XRD⟶ X-ray diffraction, HLSA⟶ high strength low alloy

The objective of the present study is to investigate the mitigation of residual stress by controlling microstructural morphologies that can elude the failures of a welded joint. Therefore, an attempt is made to understand the solidification behavior of the weld metal as well as its correlation with $\delta_{ferrite}$ formation and residual stress distribution

Table 2 Chemical composition (wt. %) of base metals

Base metals	Cr	Ni	Mo	Mn	Si	C	Fe
SS316L	18.45	8.95	2.16	1.51	0.73	0.02	Bal
SS310	25.24	19.21	0.22	0.89	1.65	0.07	Bal

% Fe). Further, EBSD analysis provides average grain size and misorientation angle distribution and allows an understanding of grain orientation in the FZ/HAZ. The measurement of residual stress (using XRD technique) at the surface of the weld joints is achieved by Bruker D8-Discover.™ system. Bragg's law is utilized to evaluate the magnitude of residual strain between atomic planes. Further, the value of stress is evaluated by the $sin^2\psi$ method, which relies on the variation of the peak location of the diffraction for different inclinations (tilt angle) of the sample [47]. The expression used for the calculation of stress by the $sin^2\psi$ method is given by [48]

$$\sigma = \frac{Y}{(1+v)} \times \frac{1}{\sin^2\psi} \times \left(\frac{d^\psi}{d^o} - 1\right) \tag{1}$$

where Y⟶ elastic modulus, υ ⟶ Poisson's ratio, ψ ⟶ angle between the bisector of the incident and diffracted rays, d^o⟶ unstrained lattice spacing, and d^Ψ⟶ strained lattice spacing. The process condition for the measurement of stress by the XRD technique is represented in Table 3.

3 Theoretical background

A 3D FE-based TMM model is developed to predict the temperature distribution, distortion, and residual stresses in dissimilar joints. The convective and radiative heat transfer from the boundary, the temperature-dependent properties (Fig. 2), and the small deformation theory are considered for distortion evaluation. The influence of shielding gas on the top surface of the melt pool is neglected and presumed to be flat. The initial temperature is considered as 303 K (ambient conditions). The governing heat conduction equation [49] is depicted as

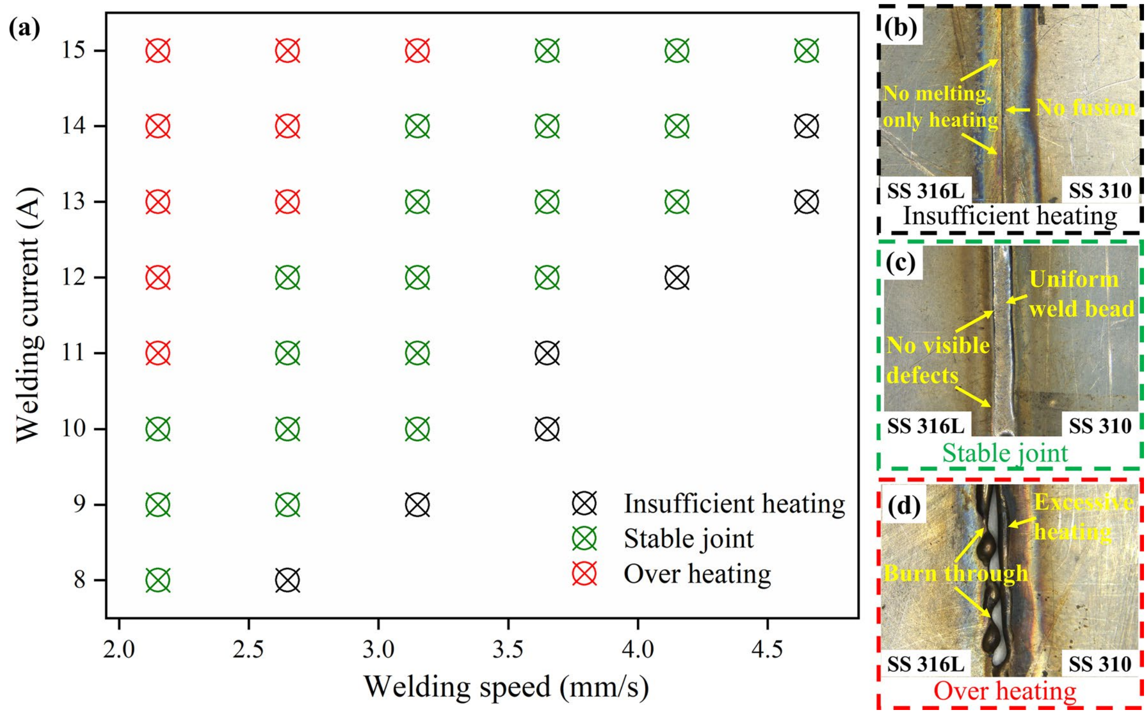

Fig. 1 **a** MPAW welding process window and **b-d** images of joints under different process parameters

Table 3 The process condition for the measurement of stress by the XRD technique

Plane	Target	Aperture (mm)	Wavelength (Å)	Voltage (kV)	Current (mA)
{311}	Cu	Square	1.54	45	14

$$\frac{\partial}{\partial x_i}\left(k_{ij}\frac{\partial T}{\partial xj}\right) + \dot{Q}_h = \rho \times C_p \times \left(\frac{\partial T}{\partial t} - V_w\frac{\partial T}{\partial x}\right) \tag{2}$$

where ρ indicates density, k_{ij} refers to thermal conductivity, $\dot{Q}_h$ implies volumetric heat generation, C_p implies specific heat, v_w is the welding velocity vector, T stands for

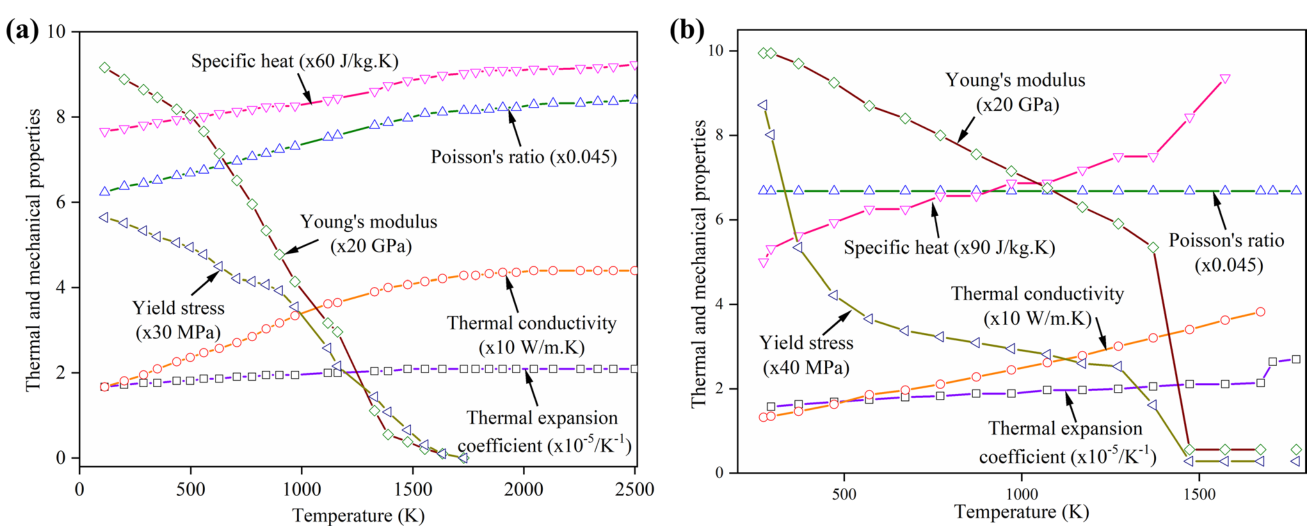

Fig. 2 Temperature-dependent properties of **a** SS310 [58] and **b** SS316L [59] were used for numerical analysis

temperature, and t indicates time. For the thermal modeling, the heat transfer coefficient and emissivity are selected as available in the literature [49]. The volumetric heat source [49] and thermal boundary conditions [49] are used in the present investigation. The volumetric heat flux is expressed as

$$\dot{Q}_h(x, y, z) = \frac{\rho_d \times \eta_{eff} \times V \times w_c}{3.14 \times r_{eff}^2 \times d} \times e\left\{-\rho_d \times \frac{(x - v_{weld}^t)^2 + y^2}{r_{eff}^2}\right\} \times e^{(h-z)}, \tag{3}$$

where p_d is the power intensity factor, V is the welding voltage, η_{eff} is the efficiency of the µ-PAW process, w_c is the welding current, r_{eff} is the effective radius of the plasma arc, d is the depth of penetration, and h is the thickness. The initial temperature is considered as ambient temperature. The heat transfer on the surface during the welding process is expressed as

$$q_{sur} = k\frac{\partial T}{\partial t}|_n + h_{conv}(T_{sur} - T_{in}) + \sigma\varepsilon(T_{sur}^4 - T_{in}^4) \tag{4}$$

where q_{sur} reflects the surface heat flux and it becomes zero to maintain an energy balance on the surface. It is to be noted that there is no input surface flux in the present case as a volumetric heat source term is included through the energy conservation equation. However, heat loss by convection and radiation is incorporated here. T_{sur} and T_{in} stand for surface and initial temperature, respectively. σ and ε illustrate the Stefan-Boltzmann constant and emissivity of the base materials. The values of the heat transfer coefficient are 30 (SS316L) and 15 (SS310) on the top surface, and 1000 on the bottom surface (due to the highly conductive fixture, made of copper). The emissivity values are used as 0.7 for SS316L) and 0.75 for SS310.

The Schaeffler and pseudo-binary illustration of the Fe–Cr-Ni ternary system accurately depicts the phase transformation behavior of FZ evolved in the dissimilar joint under various process conditions. The material under investigation undergoes a eutectic reaction that produces liquid, $\gamma_{austenite}$, and $\delta_{ferrite}$ phases at temperatures between solidus ($T_{solidus}$ ~ 1648 K) and liquidus ($T_{liquidus}$ ~ 1728 K). The present work does not consider the phase change dynamics from liquid to solid. The isopleth of the ternary Fe–Ni-Cr system (with 70 wt.% Fe) states that on the verge of SSPT, the austenitic steel comprises $\gamma_{austenite}$ and $\delta_{ferrite}$ at $T_{solidus}$. µ-PAW is categorized as a rapid cooling-assisted welding technique due to its highly collimated and coherent plasma arc. $\gamma_{austenite}$ (Ni) has a comparatively high solubility at elevated temperatures, while $\delta_{ferrite}$ is extremely stable at high temperatures. The initial phase fractions of $\gamma_{austenite}$ and $\delta_{ferrite}$ at solidus temperature are arbitrarily considered in the current work to be 4–5% and 94–95%, respectively [50]. It is assumed that the SSPT between $\delta_{ferrite} \rightarrow \gamma_{austenite}$ adheres to the John-Mehl-Avrami-Kolmogorov (JMAK) equation [51], which is written as

$$f'\gamma(T(t)) = [1 - e(-k_{\delta\rightarrow\gamma}(\tau)^n\delta \rightarrow \gamma)] \times f_\gamma^{eq} \quad (T_{\gamma s} \geq T \geq T_{\gamma f}) \tag{5}$$

where $k_{\delta\rightarrow\gamma}$ specifies the nucleation and growth rate, which primarily depends on temperature, and $f'_\gamma(T_{(t)})$ represents the phase proportion of the austenitic phase at a temperature (T) and time (t). $n_{\delta\rightarrow\gamma}$ is the Avrami coefficient to account for the nucleation, followed by growth, and $f_\gamma^{eq.}$ indicates the maximum value of the phase proportion of the γ-phase at the equilibrium stage. Further, $T_{\gamma s}$ and $T_{\gamma f}$ signify $\delta_{ferrite}$ dissolution starts (1673 K) and finish temperature (1273 K), respectively. Based on the Temperature–Time-Transformation (TTT) diagram, the highest value of transformation is assumed to be 98%, and as a result, $n_{\delta\rightarrow\gamma}$ and $k_{\delta\rightarrow\gamma}$ are estimated as 2.65 and 0.01, respectively [52].

The aforementioned empirical relation is applicable only for calculating phase proportion growth about transformation under isothermal conditions. However, to account for non-isothermal characteristics, Scheil's additivity rule is used [52]. It signifies that the total amount of time needed to attain a specified fraction of a particular phase during continuous cooling is calculated by adding several incremental isothermal steps corresponding to instantaneous temperature changes. For the incorporation of the non-isothermal behavior of phase transformation, the term fictitious time (τ_f^*) is introduced. τ_f^* is the time required for the transformation to arbitrary volume fraction, i.e., $f_{\delta\rightarrow s}$ at temperature T_o, considering an isothermal transformation at temperature $T_o + \Delta T$. Thus, τ_f^* [33, 53] is evaluated as

$$\tau_f^* = \left\{\frac{1}{-k_{\delta\rightarrow s}} \times \ln\left(1 - \frac{f_{\delta\rightarrow s}^{eqb} \times (T_o)}{f_{\delta\rightarrow s}^{eqb} \times (T_o + \Delta T)}\right)\right\}^{(N_{\delta\rightarrow s})^{-1}} \tag{6}$$

Using the Avrami model, the phase proportion at equilibrium for the transformation is displayed against temperature [51, 54] to determine the γ-phase proportion at equilibrium at a specific temperature T_t and $T_{t+\Delta t}$. Thus, by using fictitious time, Eq. (5) is changed to

$$f'\gamma(t + \Delta\tau, T + \Delta T) = \left\{ \begin{array}{l} \left[1 - e\left\{-k_{\delta\to\gamma}(\tau_o^* + \Delta\tau)\right\}^{n^{\delta\to\gamma}}\right] \times f_\gamma^{eq.} \ (1273\,K \le T \le 1673\,K) \\ 5 \times 10^{-2}\ (T > 1673\,K) \end{array} \right\} \tag{7}$$

For mechanical analysis, the static equilibrium and thermo-elastic–plastic models are considered. The governing equation for static equilibrium condition [33, 53] is written as

$$\frac{\partial S_{ij}}{\partial x_j} + f_i^b = 0 \tag{8}$$

where f_i^b represents the body force vector and S_{ij} is the Cauchy stress tensor. The stress tensor is symmetric by nature. The incremental nature of the elastic–plastic analysis is evident from the fact that total strain increment (ε_{ij}^{total}) [55] is denoted as the sum of the strain components represented by

$$\Delta\varepsilon_{ij}^{total} = \Delta\varepsilon_{ij}^{e} + \Delta\varepsilon_{ij}^{thm} + \Delta\varepsilon_{ij}^{p} + \Delta\varepsilon_{ij}^{pt} \tag{9}$$

where the components of the elastic strain ($\Delta\varepsilon_{ij}^{e}$), the thermal strain ($\Delta\varepsilon_{ij}^{thm}$), the plastic strain ($\Delta\varepsilon_{ij}^{p}$), and the phase transformation-induced strain ($\Delta\varepsilon_{ij}^{pt}$) are all listed. However, strain accompanied by other factors, including TRIP, is ignored because it shows an insignificant effect on residual stress, particularly for stainless steel [56]. The present study incorporated yield stress and associated plastic strain as a function of temperature. The plasticity model adheres to the isotropic hardening, related rate-independent flow rule, and von Mises yield criterion. The thermal and mechanical boundary conditions are represented in Fig. 3 to simulate the clamping state used in welding. The thermal strain components are algebraically added to the volumetric expansion that takes place during instantaneous phase fraction evolution corresponding to SSPT. Overall strain is composed of a thermal and a phase-transition component [33, 53] and is represented as

$$\begin{aligned} \Delta\varepsilon^{thm} + \Delta\varepsilon^{pt} &= \alpha(T) \times \Delta T + \alpha_{pt}(T,t) \times \Delta T \\ &= \Delta T[\alpha(T)] + \left\{\varepsilon^{\Delta vt} \times (T(t)) \times \Delta f'\gamma(T,t)\right\} \end{aligned} \tag{10}$$

where $\varepsilon^{\Delta vt}$ is the change in volumetric strain brought on by SSPT during the cooling stage, and $\Delta f'_\gamma$ is the instantaneous change in the phase fraction of the austenite phase. The expansion coefficient corresponding to SSPT is denoted by the symbol α_{pt}. The interaction of ferrite and austenite lattice characteristics is used to estimate the volumetric strain [33, 53], which is denoted as

$$\varepsilon^{\Delta vt}(T) = \frac{1}{3}\frac{\Delta V}{V\infty} = \frac{(V_{\delta'})^{1/3} - (V_{\gamma'})^{1/3}}{(V_{\gamma'})^{1/3}} = \frac{A_{\delta'} - A_{\gamma'}}{A\gamma'} \tag{11}$$

where $A_{\delta\prime}$ and $A_{\gamma\prime}$ represent the lattice constant of δ- and γ-phases, respectively. The $A_{\delta\prime}$ and $A_{\gamma\prime}$ [33, 53] are evaluated as

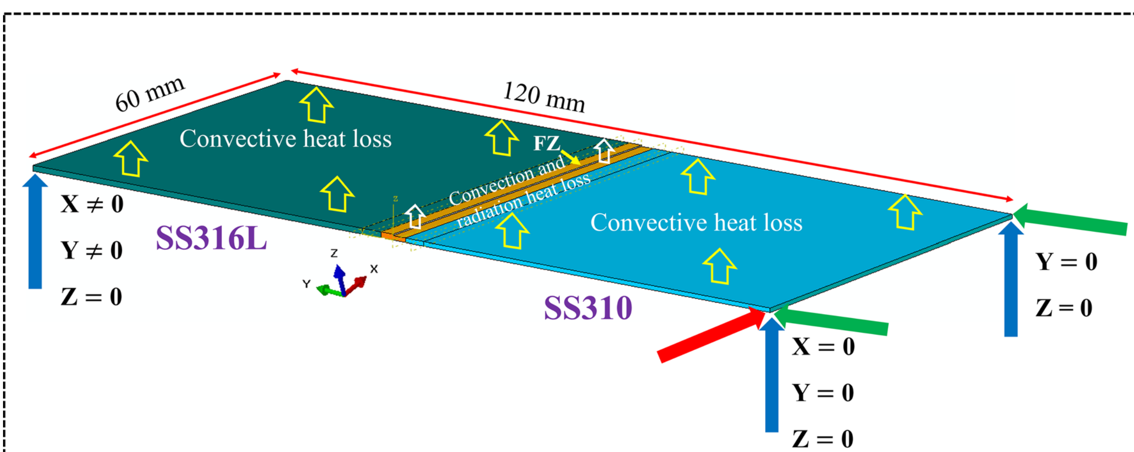

Fig. 3 Illustration of thermal boundary interaction and mechanical constraints

$$A_{\delta',\gamma'}(T) = \begin{cases} 0.28863 \times \{1 + 17.55 \times 10^{-6} \times (T - 1073\ K) \\ \{0.36308 + (0.00075 \times C\%)\} \times [1 + \{24.92 - (0.61 \times C\%)\} \times 10^{-6} \times (T - 1273K)] \end{cases} \quad (12)$$

Equation (12) is implemented to approximate the temperature-related austenite's lattice parameter, which is dependent on the percentage of carbon [57]. Carbon is a strong austenitic stabilizer and the lattice constant is highly influenced by its concentration. Overall, the volumetric strain component is used to alter the thermal strain component in structural analysis to account for the SSPT effect.

The development of a numerical model is accomplished using two separate phases. Phase I comprises of heat transfer model to extract temperature variation concerning time using the DFLUX subroutine in ABAQUS [32, 33]. Further, different temperature ranges are defined as $T < T_{solidus}$, $T_{solidus} \leq T_{melting}$, $T > T_{\delta \to f}$, and $T_{\delta,f} \leq T_{solidus}$, where $T \longrightarrow$ desired temperature, $T_{solidus} \rightarrow$ solidus temperature, $T_{melting} \rightarrow$ melting temperature, $T_{\delta \to f} \longrightarrow$ ferrite finish temperature. The mentioned temperature ranges are stated under subroutine USDFLD as state-dependent [32, 33]. The dT/dt is evaluated for the cooling phase for each node, and the node that complies with dT/dt criteria and its peak temperature corresponds to the SSPT temperature scale. This satisfying criterion displays volumetric dilation and goes through phase transformation phenomena. The output of Phase I of the numerical simulation is used as input to Phase II, in which the UEXPAN subroutine is implemented to predict the time and temperature-dependent percentage growth of $\gamma_{austenite}/\delta_{ferrite}$. After predicting the fraction of $\gamma_{austenite}/\delta_{ferrite}$, ε^{pt} is added to ε^{thm}. Further, the ε^{t} is used to evaluate residual stresses in the dissimilar joints.

The validation of the finite element (FE) model is performed using experimental measurement of temperature history, weld macrograph, residual stress, distortion, and phase fraction. These are explained in the results and discussion section. However, the calibration of the FE model requires a lot of trials including the selection of elements, extent of solution geometry, and unknown properties like convective heat transfer coefficient and mesh size. Out of these, mesh size is more sensitive to the final results. Initially, all variables are fixed except mesh size and we set the calibrated model for thermal analysis. The calibration of the model is performed with experience and data from existing literature. Here, a trade-off between mesh size and computational time is maintained to reach the optimum mesh size, which is decided to reach a constant value of peak temperature at the center of the heat source for a particular mesh size. In the present case, a mesh size of 0.2 mm is used. The elements used for the thermal and metallurgical-mechanical analysis are DC3D8 (eight-noded diffusive heat transfer linear brick element) and C3D8R (brick element accompanied by reduced integration), respectively. The number of elements and nodes selected for the present analysis are 126,000 and 141,703, respectively.

4 Results and discussion

Figure 4a–d presents a comparison between experimentally obtained micrographs and numerically simulated thermographs for L_{52} and H_{77} process conditions. The temperature contour distinguishes the fusion, mushy, and HAZ. The FZ (orange contour) is identified by $T_{liquidus}$ (1728 K), the mushy zone (red band) exists between $T_{liquidus}$ and $T_{solidus}$, and the HAZ is depicted by temperature below $T_{solidus}$. The weld geometry shows neither crater defect at the weld top nor root sagging at the bottom/root of the weld. The reliability of the developed numerical model is verified by comparing the dimensions of the top (W_{top}) and root (W_{root}) portion of the FZ. Additionally, the peak temperature obtained during the simulation is validated with the measured values by a K-type thermocouple where the limits of the inaccuracy of the thermocouple are as per ASTM E230 standard [60]. The error for the W_{top} and W_{root} is evaluated as ~ 1.77% and ~ 8.51% for the L_{52} specimen, whereas ~ 2.46% and ~ 7.21%, respectively, for case H_{77}.

Figure 4e,f compares the peak temperature for L_{52} and M_{63} conditions on either side of the dissimilar joints at a distance of 1.6 mm from the weld centerline. The error (absolute value) for the temperature data yields ~ 5.17%, ~ 5.28% (L_{52} condition), and ~ 7.43%, ~ 5.31% (M_{63} condition) on the SS316L and SS310 sides of the FZ. Figure 4g allows us to understand the variation of temperature at the top, middle, and root regions at the weld centerline for L_{52}, M_{63}, and H_{77} conditions. The peak temperature values extracted from the numerical model turn out as ~ 2032 K, ~ 2243 K, and ~ 2537 K for the cases L_{52}, M_{63}, and H_{77}, respectively. It shows a rise in the value from $L_{52} \longrightarrow M_{63} \longrightarrow H_{77}$, which is quite understandable due to the increasing amount of heat input. As the heat source moves away from a particular space, the value of peak temperature decreases. The maximum and minimum temperatures are seen at the W_{top} and W_{root}, respectively. As the heat source is in close contact at the top surface, the maximum temperature is seen at the

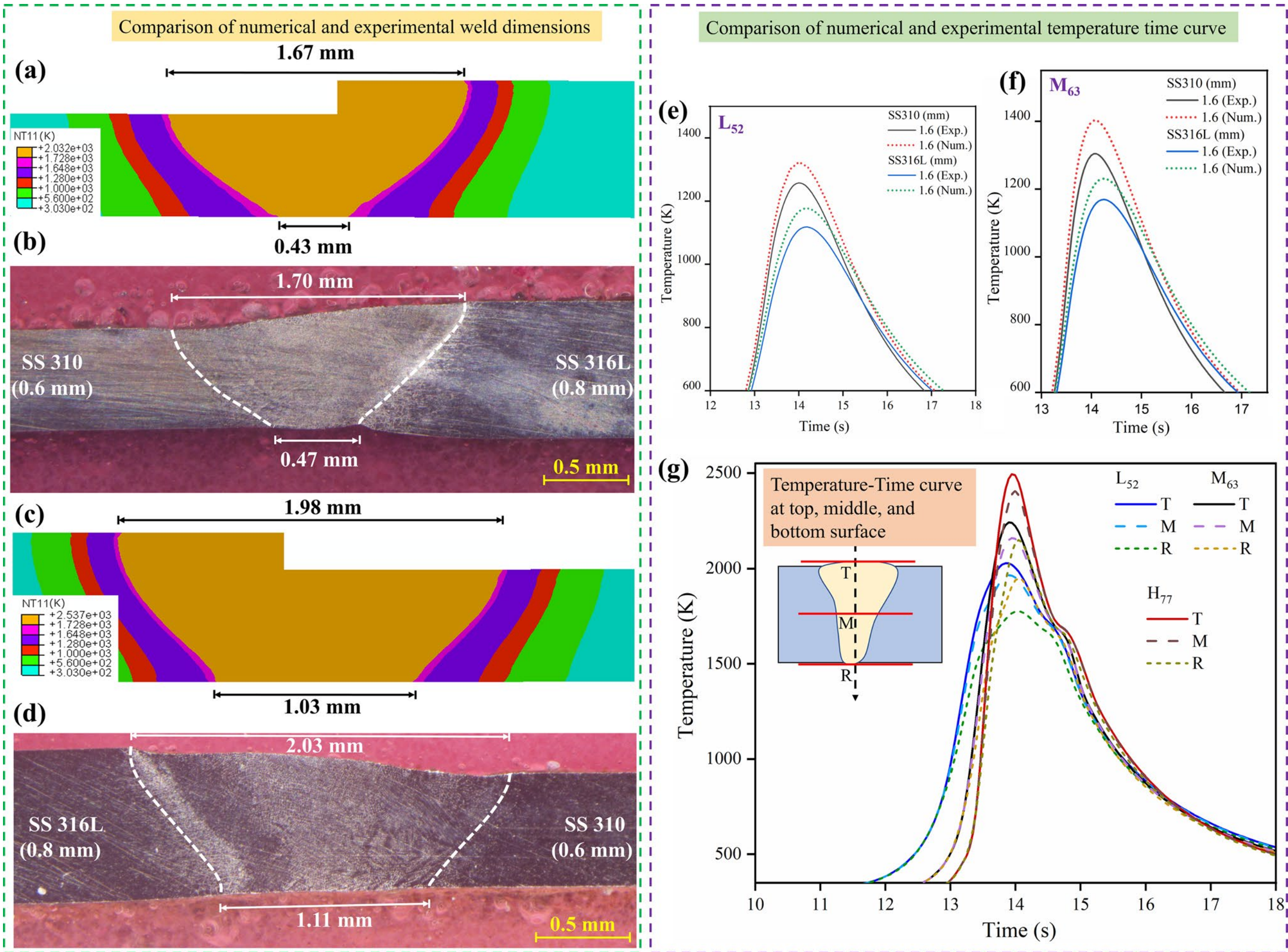

Fig. 4 **a-d** Comparison between numerically modeled and experimental weld profile for L_{52}, H_{77} process conditions, **e**,**f** compares the temperature–time history of numerical results with experimental data for L_{52}, M_{63} process conditions and **g** temperature–time profile at the top, middle, and bottom surface for L_{52}, M_{63}, H_{77} process conditions

W_{top}, whereas the minimum temperature is observed at the W_{root}, which is in contact with a highly conductive copper fixture. The time–temperature curve consists of two phases: heating and cooling. Once peak temperature is achieved, the heating phase is over, and the cooling phase begins. The cooling rate is evaluated by using the parameters G (temperature gradient) and R (growth rate). The value of G (K/mm) is extracted from the numerical model, and the value of R (mm/s) is substituted as the welding speed [61]. The value of the cooling rate ($G \times R$) is evaluated as 1063 K/s for L_{52}, 832 K/s for M_{63}, and 583 K/s for H_{77}.

The microscopic images of FZ for the dissimilar joints at L52 conditions are depicted in Fig. 5a-f. Figure 5a,b depicts the fusion boundary and FZ at the two different interfaces near the SS310 and SS316L sides. Further, in the FZ due to variations in the local cooling rate, different microstructural morphology is observed. From the fusion boundary to the center of the FZ, the cooling rate decreases; accordingly, cellular, columnar, and equiaxed structures are observed in the different regions of the FZ. In Fig. 5c–f, different areas of the FZ are shown in magnified view for clear visibility of the microstructural evolution. An equiaxed structure is evident at the weld center, followed by a columnar, and cellular structure at the fusion boundary. The FZ comprises $\delta_{ferrite}$ within the $\gamma_{austenite}$ region, and the presence of both $\delta_{ferrite}$ and $\gamma_{austenite}$ (both phases) is related to the incomplete diffusional phase transformation of $\delta_{ferrite} \longrightarrow \gamma_{austenite}$ within the FZ. The specimen associated with the high heat input condition (H_{77}) results in skeletal ferrite, whereas lathy $\delta_{ferrite}$ is observed for the lowest heat input condition (L_{52}). Different morphologies of the ferrite phase evolved due to the localized cooling rate variation in the solidified molten pool. Solidification of the melt pool governs the resulting metallurgical evolution in the dissimilar joints. To identify the mode of solidification and ferrite number in the joints, it becomes inherently necessary to calculate equivalent chromium $\left(Cr_{eq.}\right)$ and nickel equivalent $\left(Ni_{eq.}\right)$ content. An elemental analysis is carried out in the FZ,

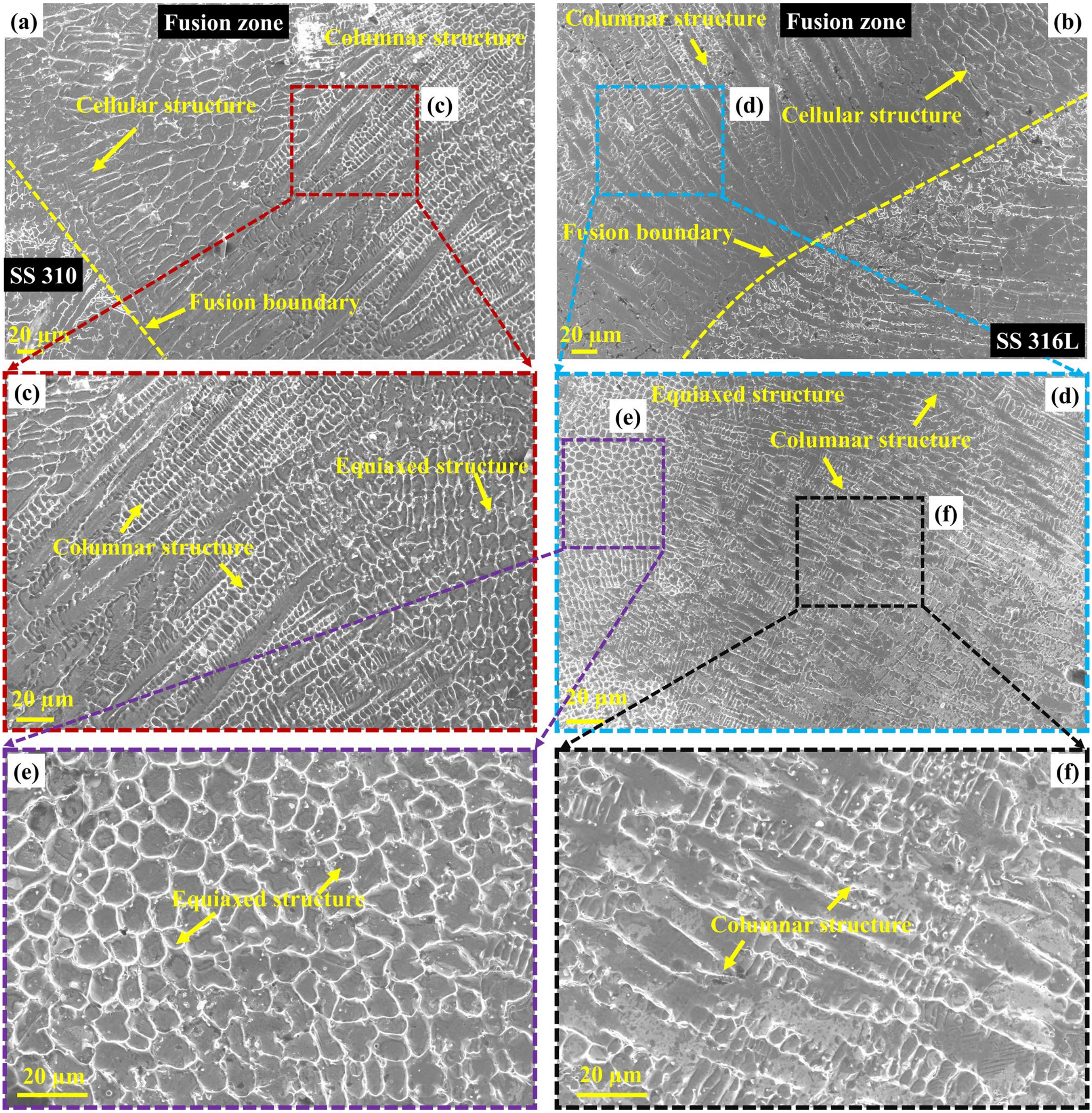

Fig. 5 **a**-**f** Presence of various microstructural morphology near the fusion boundary and in the fusion zone

and the corresponding results are shown in Fig. 6a–c. The values of $Cr_{eq.}$ and $Ni_{eq.}$ are evaluated from the elemental analysis for L_{52}, M_{63}, and H_{77} conditions. The $Cr_{eq.}/Ni_{eq.}$ ratio corresponds to the mode of solidification as austenitic (A) < 1.37, austenitic–ferritic (AF) 1.37–1.5, ferritic–austenitic (FA) 1.5–2, and ferritic (F) > 2 [62]. The estimated $Cr_{eq.}/Ni_{eq.}$ ratio is evaluated as 1.77 for L_{52}, 1.65 for M_{63}, and 1.54 for H_{77}, which is marked in the Schaeffler diagram to identify the ferrite no. and also highlighted in the pseudo phase diagram of ASS (Fig. 6d,e). Thus, from the obtained $Cr_{eq.}/Ni_{eq.}$ ratio, it is confirmed that the FZ of the dissimilar joints undergoes FA solidification mode for all three cases, leading to a dual-phase structure of ferrite (lathy) and austenite. Once the liquid melt pool starts to solidify, after 1728 K, the molten pool comprises liquid metal (*L*) and $\delta_{ferrite}$ (δ). On reaching 1648 K, along with *L* and δ, it also shows γ-phase. On complete solidification, *L* completely transforms into δ and γ phases. After solidification,

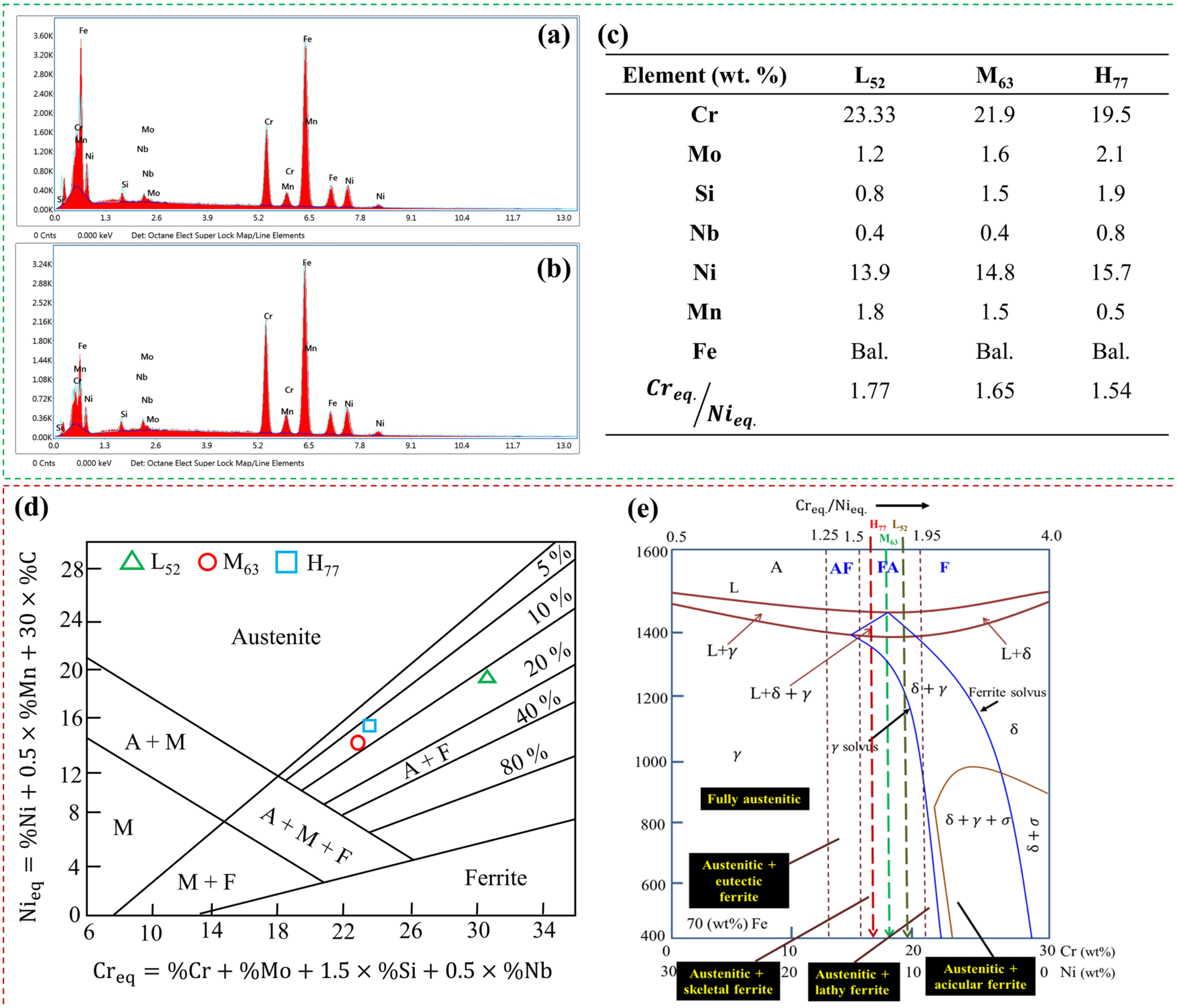

Element (wt. %)	L_{52}	M_{63}	H_{77}
Cr	23.33	21.9	19.5
Mo	1.2	1.6	2.1
Si	0.8	1.5	1.9
Nb	0.4	0.4	0.8
Ni	13.9	14.8	15.7
Mn	1.8	1.5	0.5
Fe	Bal.	Bal.	Bal.
$Cr_{eq.}/Ni_{eq.}$	1.77	1.65	1.54

Fig. 6 **a**,**b** depicts elemental analysis, **c** chromium and nickel equivalent calculation, the composition of dissimilar joints represented on **d** Schaeffler diagram; **e** pseudo phase diagram of ASS [50]

the retained $\delta_{ferrite}$ ranges from 7 to 12% for the conditions L_{52}, M_{63}, and H_{77}.

Figure 7a–c illustrates point, line, and area mapping analysis for selected regions in the FZ for sample L_{52}. In Fig. 7a, point elemental analysis is carried out for two spectrums: the first point (spectrum 1) is selected inside the austenitic region, and the second (spectrum 5) is selected in the dendritic ferrite region. Ni is an austenitic stabilizer, and Cr is a ferritic stabilizer; therefore, the elemental analysis indicates the predominant variation of Cr and Ni in the austenitic and dendritic regions. The austenitic region shows higher Ni content, whereas the dendritic region shows higher Cr content. It is observed that phase transformation from $\delta_{ferrite} \longrightarrow \gamma_{austenite}$ relies on diffusion, with pct. of Cr increasing from ~ 19% (austenitic region) to ~ 25% (dendritic region), and pct. of Ni decreasing from ~ 14% (austenitic region) to ~ 9% (dendritic region). Figure 7b illustrates the line elemental analysis for a selected length of 100 μm, in which the variation of all the elements can be observed, especially Cr and Ni. A peak in the Cr line (pink color) can be observed as it crosses the dendritic region, whereas a peak in the Ni line (cyan color) can be seen as it passes through the austenitic matrix. Iron (Fe) is present in maximum pct.; thus, red (color) remains at the top. Figure 8a-b, e–f illustrates the base metals (BM) (SS310, SS316L), HAZ, FB, and FZ; Fig. 8c-d, g-h presents the line spectrum at the interface of the weld joints for a better understanding of the elemental diffusion across the FZ, HAZ, and BMs. The line spectrum shows consistency in the elemental analysis with no

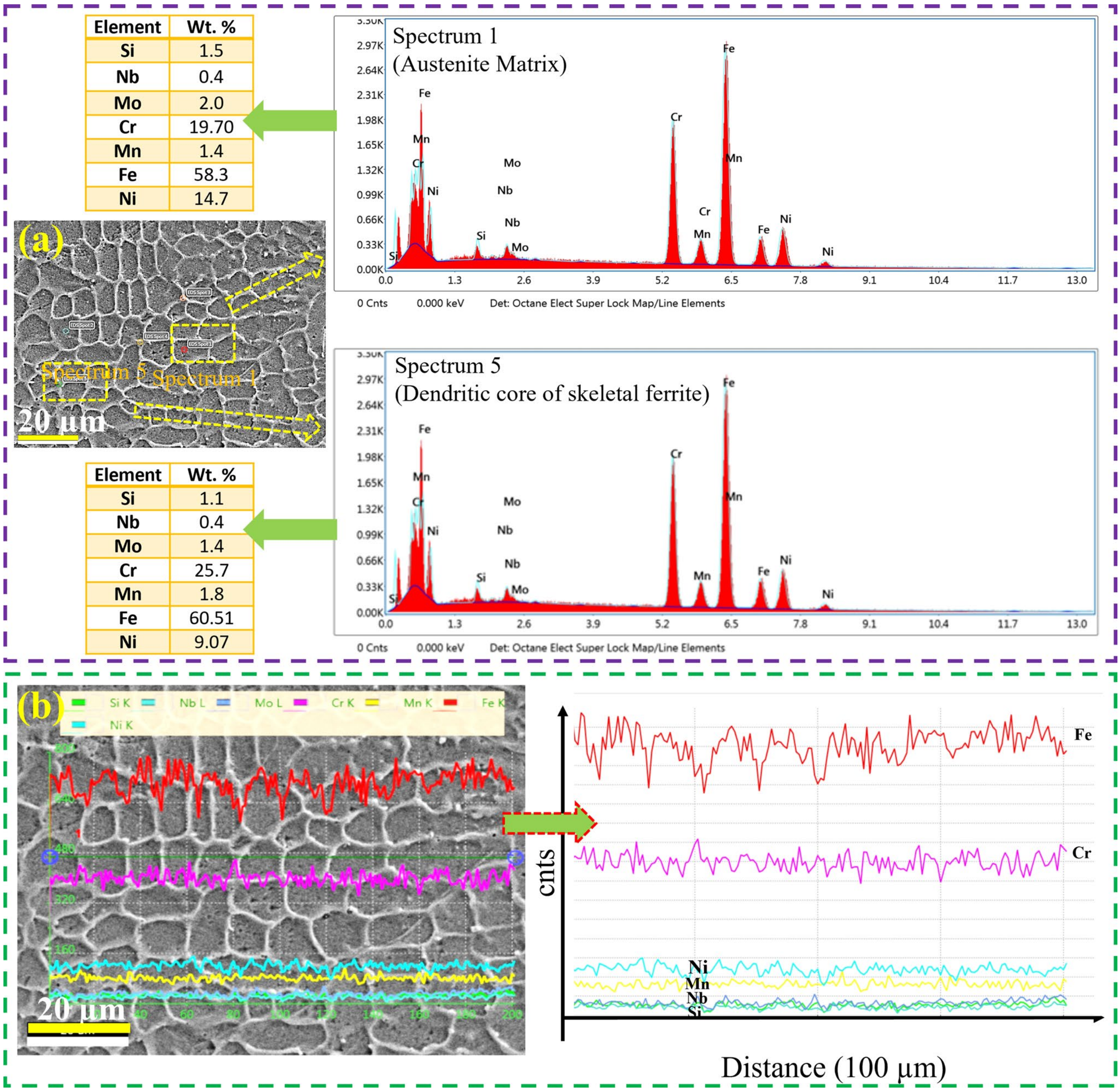

Fig. 7 Illustrates **a** point spectrum, and **b** line spectrum in the weld center of the fusion zone

significant rise/sudden drop in the major elements like Fe, Cr, and Ni.

The elements Cr and Ni act as ferritic and austenitic stabilizers, respectively. An increase in Cr and a decrease in Ni content is related to the rejection of Cr and absorption of Ni in the austenitic region. Thus, complete transformation fails to occur during the solidification process at a high cooling rate. This incomplete transformation forces $\delta_{ferrite}$ to be partially transformed into $\gamma_{austenite}$. The complete physics of the process is explained in Fig. 9. The process starts with the equiaxed grain structure of the base metal (Fig. 9a). The process follows the heating, solidification, and cooling stages. Figure 9b illustrates solidification stages for L_{52} and H_{77} conditions, wherein FA solidification prevails. The solidification stages for L_{52} and H_{77} conditions can be stated as: $L \rightarrow L + \delta \rightarrow L + \delta + \gamma \rightarrow \delta + \gamma$. During the$L + \delta$ stage, a high cooling rate (1063 K/s) results in the formation of more amount of $\delta_{ferrite}$ in the L_{52} condition compared to a low cooling rate (583 K/s) in the H_{77} condition. Just before $T_{solidus}$, $L + \delta + \gamma$ a mixture exists together for a short-lived period. The formation of $\gamma_{austenite}$ results from the complete transformation of $\delta \longrightarrow \gamma$. As shown

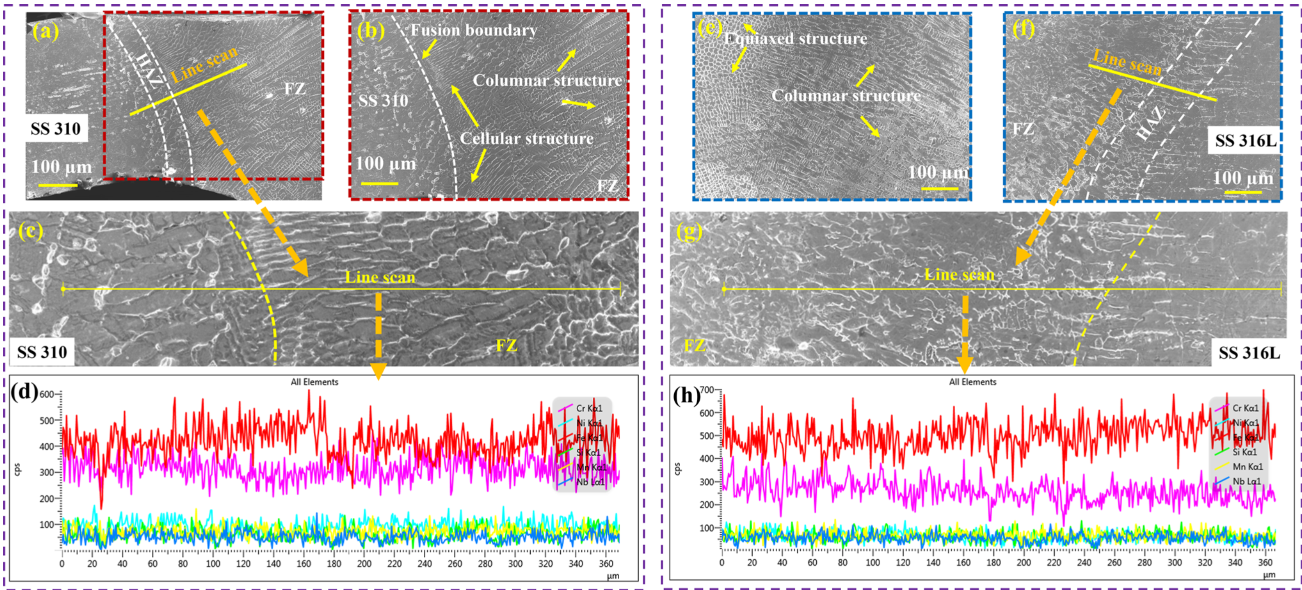

Fig. 8 **a-b**, **e–f** Microstructure of base metals: HAZ, fusion boundary, and fusion zone; **c-d**, **g-h** represents the line spectrum at the interface of the weld joint for the L_{52} process condition

in Fig. 9b, the transformation of $\delta \longrightarrow \gamma$ is caused by the combination of Cr in the dendritic region and the dissociation of Ni from the austenitic matrix. In the final stage, the temperature reaches from $T_{solidus}$ to T_{room}, which results in a microstructure comprising both phases ($\delta + \gamma$). Here, the lathy and skeletal shape pattern $\delta_{ferrite}$ is identified. Figure 9c shows the completely transformed austenitic matrix with enriched dendritic core ferrite boundary. Figure 9d illustrates the complete transformation ($\delta \longrightarrow \gamma$) and the existing variation in the elemental composition of the dendritic core and austenitic region. Due to the presence of $\delta_{ferrite}$ in the dendritic core region, the percentage of Cr is high, whereas in the austenitic region, Ni content is high.

The influence of heat input on microstructural morphology is observed in Fig. 10a–d. Irrespective of the heat input, lathy and skeletal shape pattern $\delta_{ferrite}$ are identified. However, the relative amount of lathy $\delta_{ferrite}$ is directly proportional to the cooling rate. In Fig. 10a,b, the lath size for the dendritic arms is shown in blue color, the $\delta_{ferrite}$ is represented in maroon color arrows, and the $\gamma_{austenite}$ matrix is shown in yellow color arrows for L_{52} and H_{77}. The figure also depicts inter-dendritic or primary dendritic arm spacing (PDAS) and secondary dendritic arm spacing (SDAS). Figure 10c depicts the FZ, fusion boundary, and the heat-affected region for the L_{52} condition; Fig. 10d shows the enlarged view in the FZ, wherein the presence of lathy $\delta_{ferrite}$ can be observed. The measurement (average value) of $\delta_{ferrite}$ lath size reveals 412 nm (L_{52}), 723 nm (M_{63}), and 1040 nm (H_{77}). It is to be noted that the low heat input (high cooling rate) condition allows limited time for the overall growth of lath size, whereas high heat input allows sufficient time for the growth of dendrites; a similar trend has been reported earlier [63]. The inter-dendritic spacing (average) measures ~ 10 µm (L_{52}), ~ 15 µm (M_{63}), and ~ 20 µm (H_{77}). It is to be noted that the value of inter-dendritic spacing also shows an increasing trend with an increase in heat input [64].

During the cooling phase, the initial phase fractions of $\gamma_{austenite}$ and $\delta_{ferrite}$ at $T_{solidus}$ are arbitrarily considered as 4–5% and 94–95%, respectively [35]. During solidification, once the temperature falls below $T_{solidus}$, unstable $\delta_{ferrite}$ goes into the $\gamma_{austenite}$ matrix due to elemental diffusion, wherein the crystal structure changes from BCC ($\delta_{ferrite}$) to FCC ($\gamma_{austenite}$). The BCC $\longrightarrow$ FCC transformation corresponds to volumetric enlargement; thus, the proportion of ferrite decreases, and the amount of austenite increases. The complete phase transformation ($\delta_{ferrite} \longrightarrow \gamma_{austenite}$) fails to occur below 1273 K (γ finish temperature), and some ferrite content is retained in the FZ, which remains as retained ferrite. Figure 11a-c illustrates the transformation of $\delta_{ferrite} \longrightarrow \gamma_{austenite}$ and retained ferrite concerning temperature and time. The slope of the phase diagram for the experimental and numerical conditions shows a considerable variation due to the high cooling rate achieved in the FZ. The percentage of retained ferrite using the numerical model is predicted as ~ 13.1% for L_{52}, ~ 11.2% for M_{63}, ~ 8.8% for H_{77}, and the remaining fraction comprises an austenite matrix in the FZ. Figure 11d shows a quite satisfactory comparison between numerical results and the data determined from the Seferian relation [50].

Figure 12 depicts the FESEM spectrum of the solidified weld zone along with calculated $\delta_{ferrite}$ volume fraction at three different heat inputs. A Gaussian blur is applied before

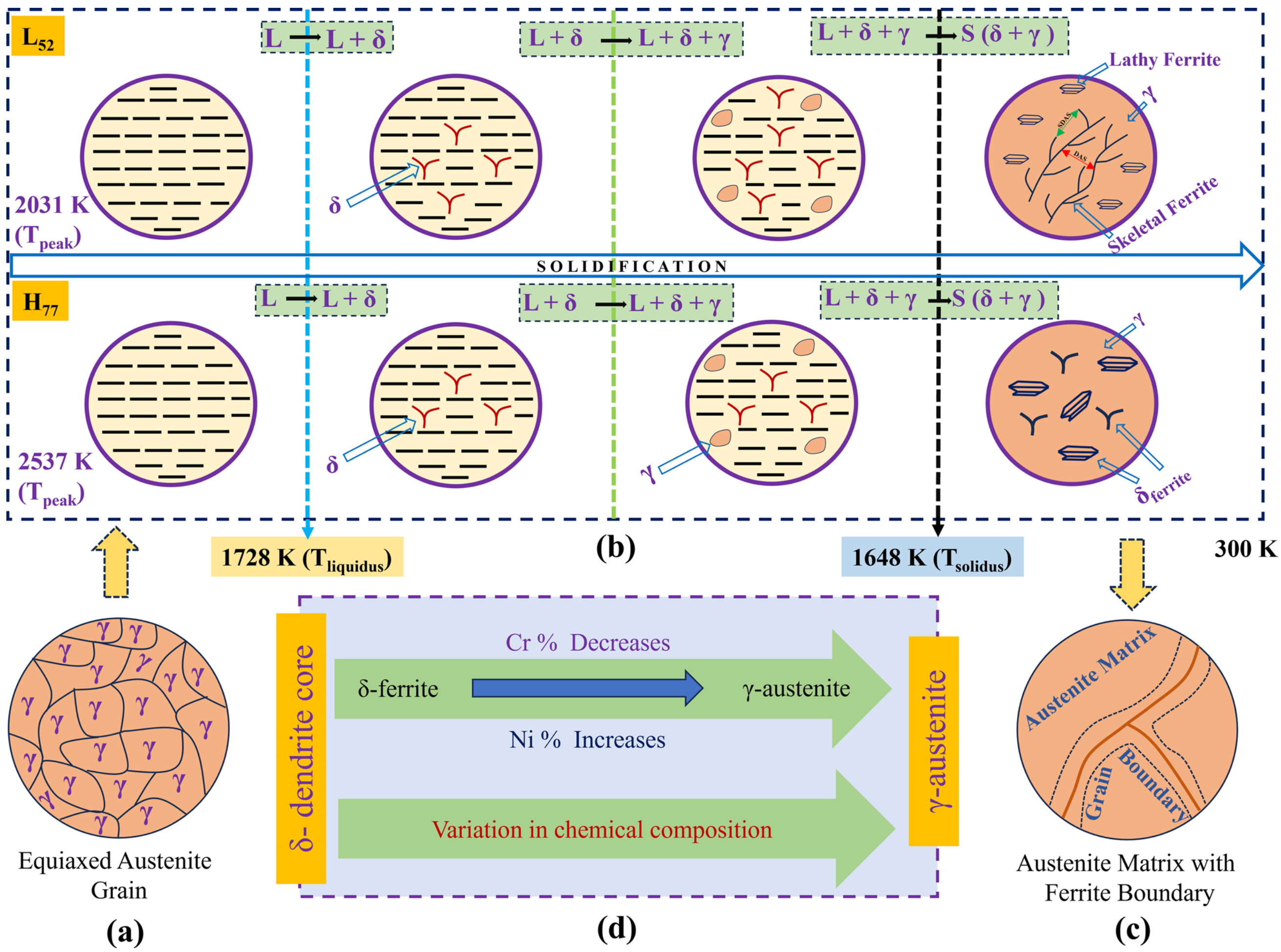

Fig. 9 Illustrates **a** equiaxed γ-grains, **b** schematic representation of microstructural changes for L_{52} and H_{77}, **c** austenitic matrix with ferrite enriched dendritic core, and **d** shows the variation of Cr and Ni in austenitic and dendritic region

applying a manual threshold to determine the volume pct. of the $\delta_{ferrite}$ phase. This comprises converting an unprocessed image (RGB) to a greyscale (8-bit) image, which is then thresholded to generate a binary (black and white) image. Accordingly, the $\delta_{ferrite}$ is identified as white-branched skeletons in the black region (matrix), as depicted in Fig. 12b. The fraction measurements are performed using the standard manual point count method [65], in which a grid of points is superimposed on the microstructural images illustrated after thresholding using ImageJ software. The ratio of the total number of points occurring in the phase that is of interest to the total available number of grid points is obtained, and this ratio yields the estimated statistical value of the phase in volume fraction. The dual-phase microstructure clarifies the incomplete phase transformation from $\delta_{ferrite}$ to $\gamma_{austenite}$. Figure 12c, d displays dampening of skeletal-structured $\delta_{ferrite}$ phase fraction from 11.2% → 7.9% upon increasing heat input from 52 → 77 J/mm. Higher heat input provides the platform for the dissolution of $\delta_{ferrite}$ into the $\gamma_{austenite}$ matrix, which leads to the diffusional transformation of $\delta_{ferrite} \rightarrow \gamma_{austenite}$. The error in the numerically predicted values of $\delta_{ferrite}$ concerning experimental values is evaluated as ~ 16% for L_{52}, ~ 15% for M_{63}, and ~ 11% for H_{77} process conditions.

Figure 13a illustrates the XRD pattern of the FZ, and the intensity counts are depicted in Fig. 13b. The planes (111), (200), (220), and (222) represent $\gamma_{austenite}$ peaks, and the plane (110) corresponds to $\delta_{ferrite}$ peak. Intensity counts (intensity peak) directly relate to the quantity of phases available in the inspected region [66]. The intensity counts of the γ (111), γ (200), γ (220), γ (222), and δ (110) show a decreasing trend as the heat input increases. The decreasing intensity of the γ-phase is related to incomplete transformation ($\delta_{ferrite} \longrightarrow \gamma_{austenite}$), which is elaborated under the mode of solidification section in Fig. 9. The case of δ (110) also shows a decreasing trend with increasing heat input. The highest count is observed for the case L_{52} (~ 1063 K/s). The time availability for conversion of $\delta_{ferrite} \longrightarrow \gamma_{austenite}$ is

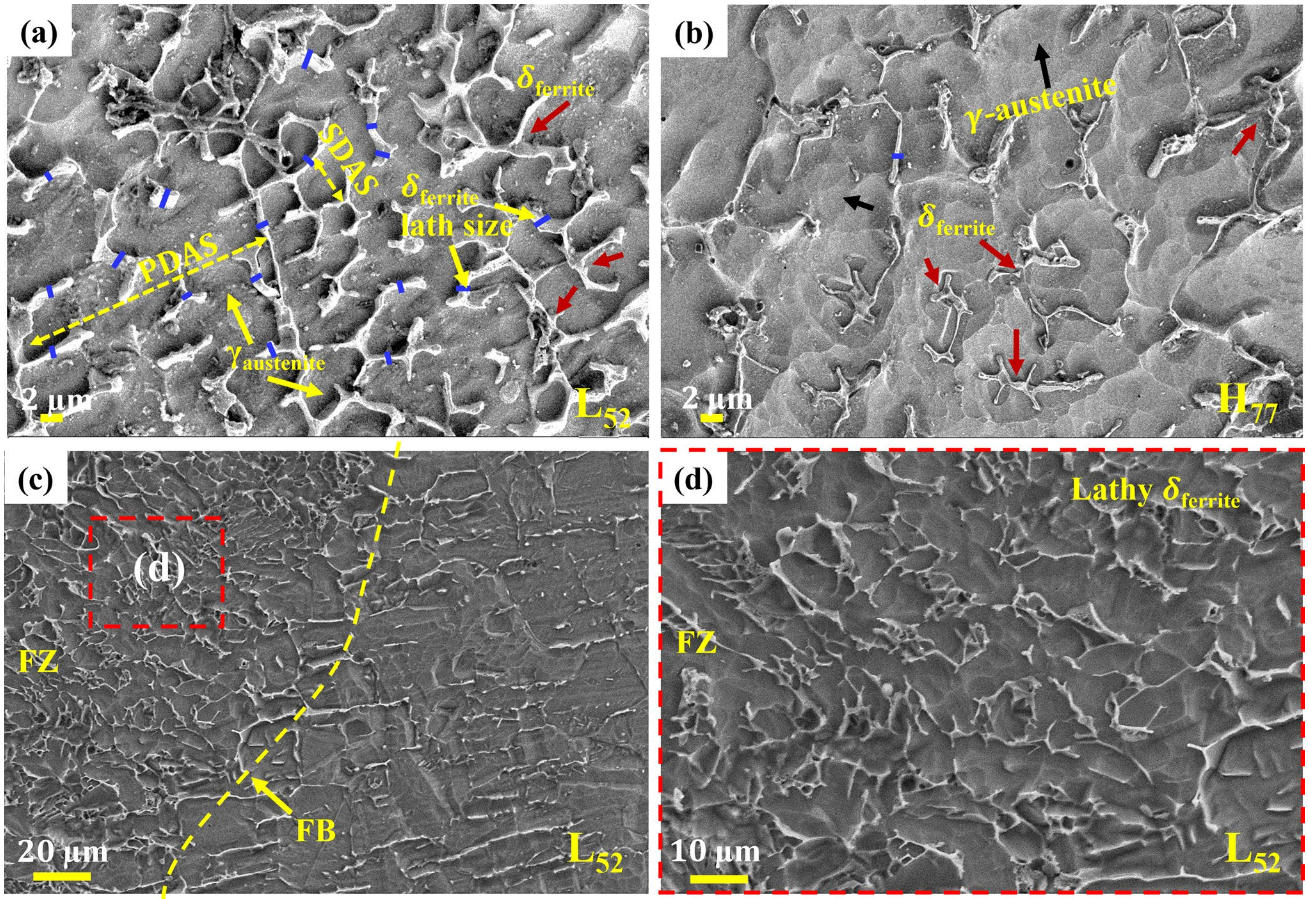

Fig. 10 Microstructural morphology for different process conditions **a** L_{52}, **b** H_{76}, **c-d** L_{52}

less for a high cooling rate and hence, the amount of $\delta_{ferrite}$ enhances with an increase in the cooling rate [33].

EBSD analysis for the base metals and the FZ at different process conditions is conducted, and the variation of grain size with inverse pole figure (IPF) maps is depicted in Fig. 14. The IPF maps of the base metals are depicted in Fig. 14a. It provides the grain size variation throughout the area fraction, from 1.39 μm to 37.06 μm for SS316L and from 1.39 μm to 45.89 μm for SS310. The average grain size for the base metals is 7.42 μm for SS316L and 9.63 μm for SS310. Figure 14b depicts the fluctuation in grain size with heat input, where a rise in heat input results in increased grain size. An increase in heat input leads to a slower cooling rate, which provides more time for the grains to grow. The increase in grain size can be observed from the IPF maps, where the grain diameter varies from 3.55 μm to 211.71 μm for L_{52}, 2.87 μm to 247.22 μm for M_{63}, 5.65 μm to 426.27 μm for H_{77}. The average grain size is evaluated as 28.68 μm for L_{52}, 42.57 μm for M_{63}, and 58.53 μm for H_{77}. Figure 14b also illustrates the IPF maps for all three cases, L_{52}, M_{63}, and H_{77}. Further, the enlarged view of IPF maps for L_{52}, M_{63}, and H_{77} conditions is shown in Fig. 14c–e. Figure 14f,g denotes the misorientation angle and the frequency with which it occurs. It enables us to understand the presence of low-angle grain boundaries (LAGBs, $2^{\circ} < \theta < 15^{\circ}$), and high-angle grain boundaries (HAGBs, $15^{\circ} < \theta < 65^{\circ}$) [67]. The LAGB and HAGB are relatively similar for the base materials, whereas LAGB and HAGB vary with heat input. The pct. of LAGBs increased ($23.64 \longrightarrow 38.16 \longrightarrow 48.99\%$), and HAGBs decreased ($76.36 \longrightarrow 61.48 \longrightarrow 51.01\%$) with an increase in the heat input value. Thus, it can be concluded that an increase in heat input value leads to a decrease in HAGBs. The relative decrease in HAGBs or increase in LAGBs results from a high cooling rate. As the solidification rate decreases, the FZ is in a state of extreme non-equilibrium, corresponding to the formation of high-density LAGBs [68, 69]. Also, fatigue resistance positively correlates with residual stress value; in other words, low-density LAGBs lead to a lower value of stresses developed [70, 71].

The estimated residual stress obtained from the numerical results is validated with the experimental values, and a comparison is made in Fig. 15a,b at three heat input conditions. The longitudinal component (S11) of residual stresses

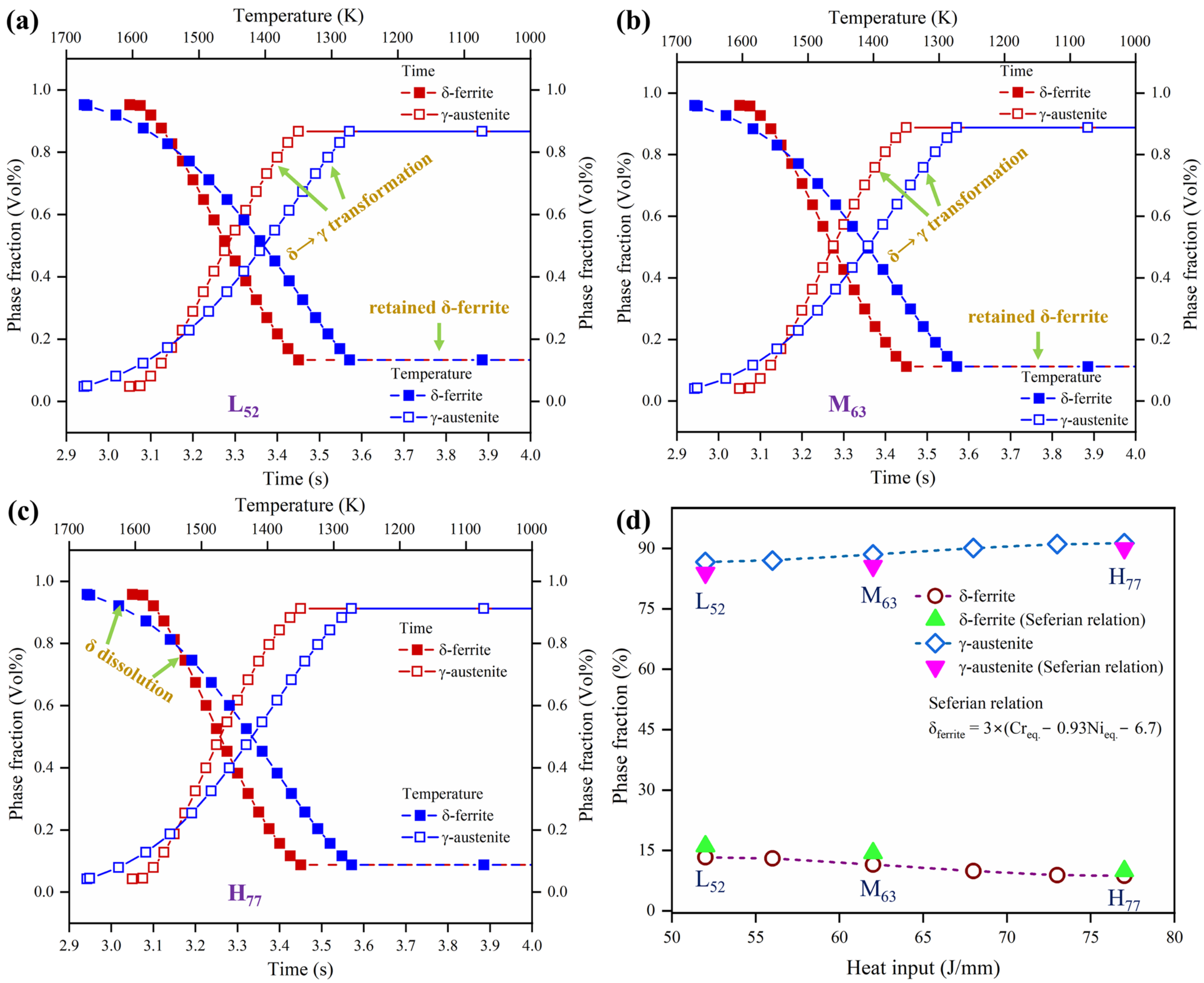

Fig. 11 Illustrates $\delta_{ferrite} \rightarrow \gamma_{austenite}$ transformation for different process conditions **a** L_{52}, **b** M_{63}, and **c** H_{77}; **d** compares $\delta_{ferrite}$ and $\gamma_{austenite}$ fraction numerical results with Seferian relation

against the distance across the weld cross-section is presented in Fig. 15a. The numerically calculated S11 stress values are 212, 239 and 280 MPa, where the pct. error in predicting the S11 stress value is evaluated as ~ 17% for L_{52}, ~ 11% for M_{63}, and ~ 15% for H_{77} process conditions. As the heat input increases from L_{52} to H_{77}, a high rise of 147.3 MPa is observed because high heat input (H_{77}) leads to more melting of the base materials, leading to larger contraction, and higher values of residual stresses. In contrast, low heat input corresponds to lower melting of the base materials, which confines the FZ to a narrower region, thus leading to a lower value of residual stress. The S11 stress changes from positive (tensile) at the weld center line and nearby location to negative (compressive) at a faraway location i.e., at a distance of ~ 5 mm from the weld center line for the L_{52} condition. As the heat source moves away, the heated region starts to cool down and regain its length, wherein positive (tensile) stresses are developed [72]. The maximum magnitude of the longitudinal stress field (S11) is measured as ~ 181 ± 38 MPa at the fusion line, whereas it is obtained as ~ 266 ± 34 MPa and ~ 328 ± 20 MPa for specimens M_{63} and H_{77}, respectively. The localization in the distribution of tensile residual stress is also seen by a highly collimated micro-plasma beam, which resulted in a relatively low cooling rate and less temperature gradient at distant locations across the weld region for the lowest heat input condition (L_{52}). The maximum compressive residual stress (S11) of 88 ± 30 MPa (SS310 side) and 94 ± 33 MPa (SS316L side) at location ~ 11 mm is seen for case L_{52}; however, it is measured as 144 ± 35 MPa (SS316L side) and 122 ± 34 MPa (SS310 side) for M_{63} sample and 165 ± 34 MPa (SS310 side) and 183 ± 28 MPa (SS316L side) for case H_{77}.

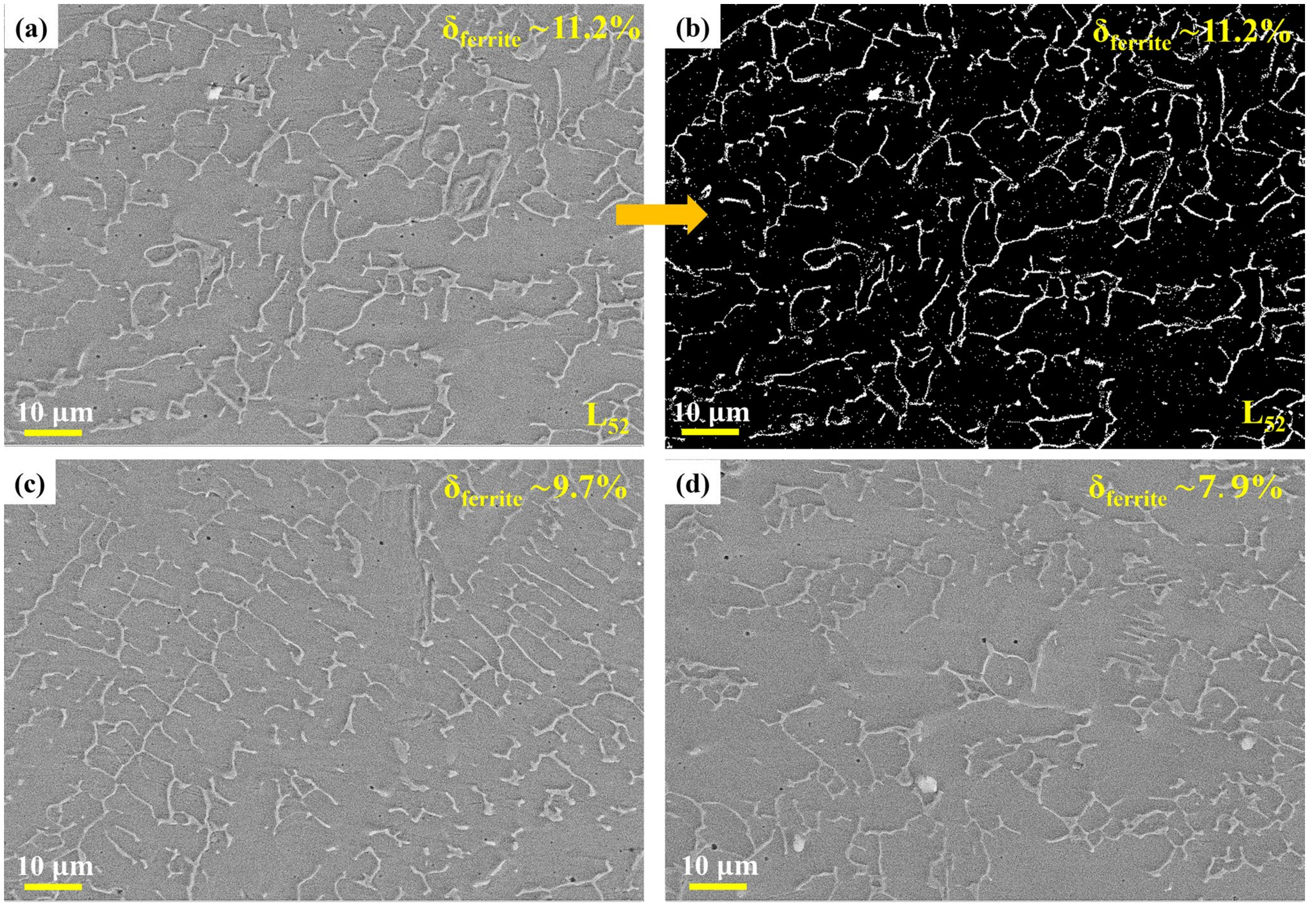

Fig. 12 Retained pct. of $\delta_{ferrite}$ for different process parameters **a**, **b** L_{52}, **c** M_{63}, and **d** H_{77}

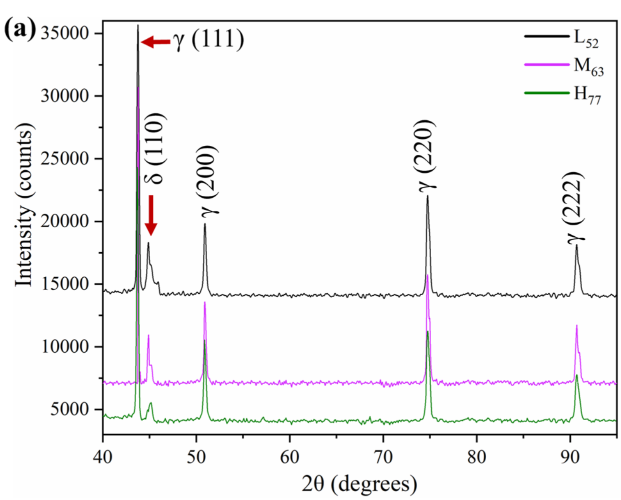

(b)

Process conditions	L_{52}	M_{63}	H_{77}
$\delta_{ferrite}$ (110)	18976	10964	5539
$\gamma_{austenite}$ (111)	37701	30699	27580
$\gamma_{austenite}$ (200)	20547	13887	10112
$\gamma_{austenite}$ (220)	22201	15368	12012

Intensity counts

Fig. 13 **a** XRD pattern in the FZ for L_{52}, M_{63}, and H_{77} process conditions, and **b** intensity counts for $\delta_{ferrite}$ and $\gamma_{austenite}$

The tensile stress at the nearby location of the weld region is compromised by successive compressive stress at a distant location to maintain the neutrality of the structural stress field or to accommodate structural equilibrium. Figure 15b illustrates the comparison in the residual stress values along the transverse direction (perpendicular to the weld direction, S22). The S22 stress (transverse) value is relatively smaller than the S11 component. The S22 stress values also

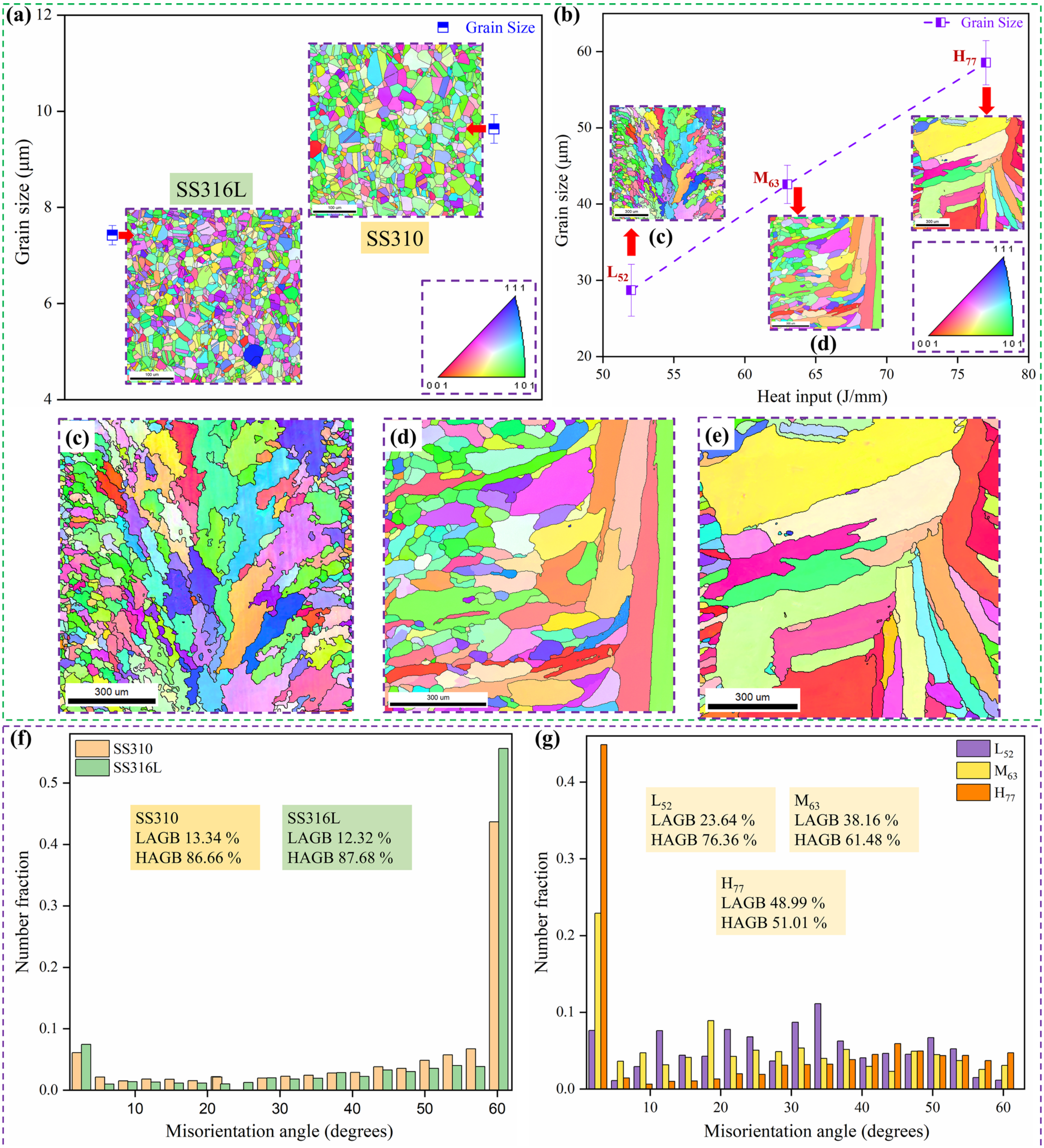

Fig. 14 Grain size and IPF maps for **a** base metals, **b** at different heat inputs L_{52}, M_{63}, and H_{77}, **c**–**e** IPF maps for L_{52}, M_{63}, and H_{77} and **f-g** misorientation distribution

show a similar trend as S11 stress, wherein, residual stresses also increase with the increase in the heat input value. The value of S22 stress is experimentally determined as − 19.5 ± 10 MPa, 67.3 ± 23 MPa, and 124.6 ± 32 MPa for L_{52}, M_{63}, and H_{77} conditions, respectively. The S22 stress value primarily relies on the size of the FZ, i.e., a smaller width of the FZ achieved under low heat input conditions lowers the stress value alongside changing the nature of stress [73]. The S22 value for L_{52} changes its value from negative (compressive) at the weld center line to zero at the outer edges.

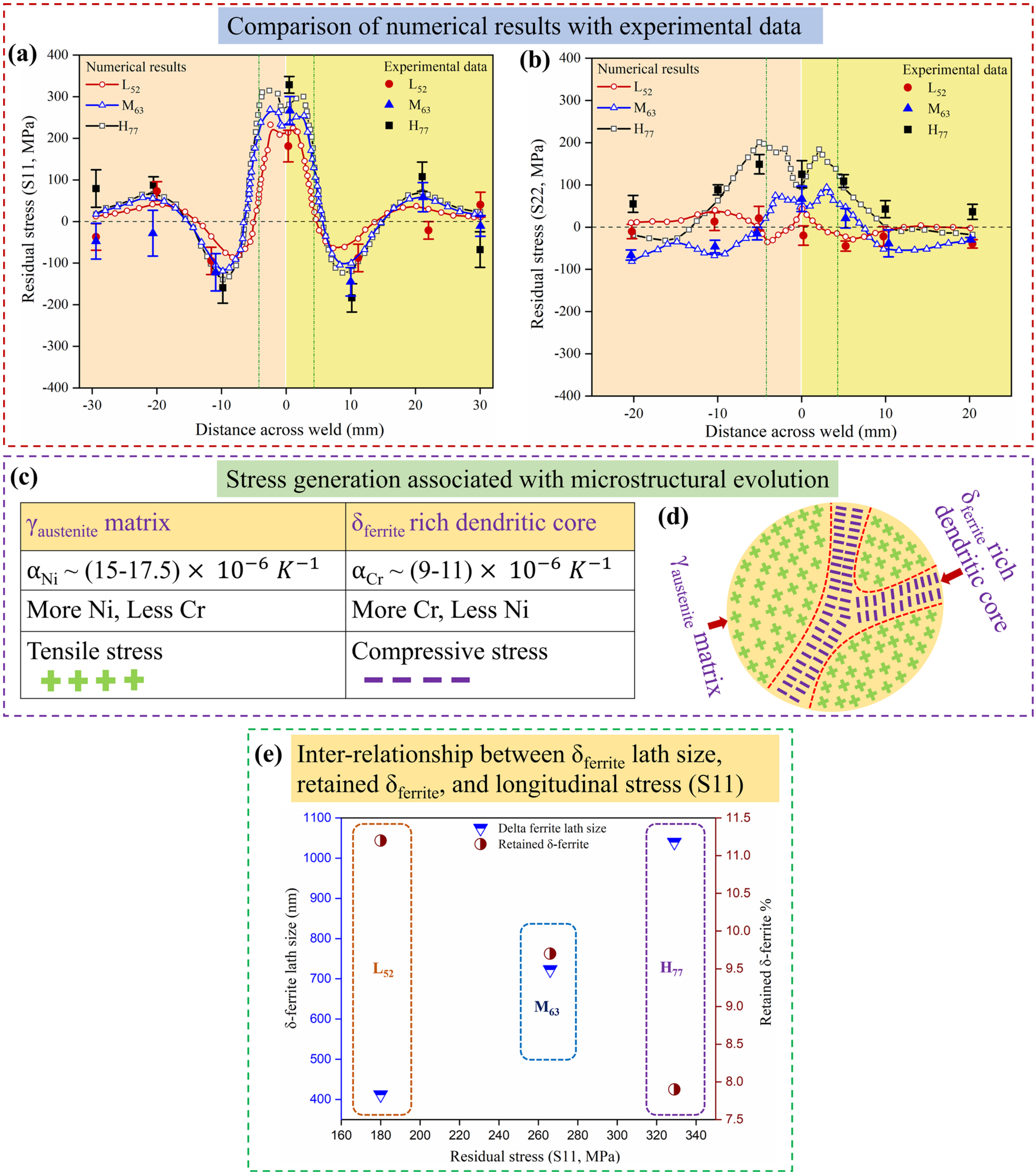

Fig. 15 **a**-**b** Comparison of residual stresses developed along the longitudinal (S11) and transverse direction (S22), **c** tensile/compressive stress generation, and **d** inter-relation between lath size, longitudinal stress, and retained $\delta_{ferrite}$ pct. for L_{52}, M_{63}, and H_{77} conditions

The highest value of S11 (328.6 ± 20 MPa) and S22 (124.6 ± 32 MPa) stress components correspond to the maximum heat input condition (H_{77}), whereas the minimum heat input condition (L_{52}) results in relatively low stress (S11 and S22) value.

The FZ for the L_{52} condition comprises 11.2% $\delta_{ferrite}$ and 88.8% γ-austenite, and for the H_{77} condition comprises 7.9%

$\delta_{ferrite}$ and 92.1% $\gamma_{austenite}$. Figure 15c presents the stress generation in the $\gamma_{austenite}$ region and $\delta_{ferrite}$ core regions in a tabular format. The presence of higher $\delta_{ferrite}$ involves more amount of Cr and less Ni content. Also, it is to be noted that the austenitic matrix comprises higher Cr and less Ni content, whereas $\delta_{ferrite}$ contains higher Ni and less Cr content, and the coefficient of thermal expansion (α), for Ni is ~ 1.6 times that of Cr [33, 74]. Due to the difference in the value of α, the γ-region (containing more amount of Ni) contracts more as compared to the δ-region (containing more amount of Cr), which corresponds to compressive stresses in the dendritic core region and tensile stresses in the γ-region. Figure 15d illustrates the tensile and compressive stress behavior associated with the γ-region and $\delta_{ferrite}$ core region, respectively. The reduction of tensile stresses in the FZ for L_{52} and M_{63} conditions is observed. Under the high heat input condition (H_{77}), lower $\delta_{ferrite}$ content restricts compressive stresses in the FZ. Also, the deformation of $\delta_{ferrite}$ is restricted by the surrounding hard phase austenite, which restricts the development of back stress due to $\delta_{ferrite}$, thus resulting in a lower stress level for L_{52} than the H_{77} condition. It suggests that residual stress distribution is changing mostly due to volumetric changes during phase transition, which might greatly reduce the cumulative longitudinal stress. Hence, an increase in lath size (412 nm for L_{52} to 1040 nm for H_{77}) and an increase in inter-dendritic spacing (10 µm for L_{52} to 20 µm for H_{77}) also aid in the overall enhancement of the value of locked-in stress. Figure 15e shows the inter-relationship between $\delta_{ferrite}$ lath size and retained $\delta_{ferrite}$ on the resulting S11 stress value. It is observed that a lower value of lath size (412 nm) and higher retained $\delta_{ferrite}$ pct. (11.2%) leads to a minimum S11 value (181.3 ± 38 MPa). Overall, a low heat input value, higher retained $\delta_{ferrite}$, fine lath size, and reduced inter-dendritic spacing lead to minimum residual stress value [6, 10].

Figure 16 represents the longitudinal (S11) stress for L_{52}, M_{63}, and H_{77} conditions. The presence of tensile stress near the weld region for all the cases is obvious. Further, to maintain structural equilibrium, the tensile (positive) nature of the stress changes to compressive (negative) for the region away from the FZ. The maximum value of residual stress for L_{52} and M_{63} cases is identified as 235.7 and 269.7 MPa, respectively, which falls within the yield strength value of the base metals (277 MPa for SS310 [75] and 376 MPa for SS316L [76]). In contrast, the value of residual stress is estimated as 315.7 MPa for the H_{77} condition, which is on the higher side with reference to the base material SS310. It indicates a severe chance of structural failure on the SS310 side.

The effect of phase transformation is also observed in the resulting distortion value of the steel joints. To evaluate the influence of phase transformation, the distortion value is analyzed for dissimilar joints fabricated at maximum heat input conditions (H_{77}). Figure 17a-b illustrates distortion along the weld direction and out-of-the-plane distortion for the H_{77} condition. An outward convex-type shape along the weld (longitudinal, U_x) direction indicates that the maximum deflection occurs near the center, and the minimum deflection occurs at the edges. The maximum deflection (U_x) with and without consideration of phase transformation is

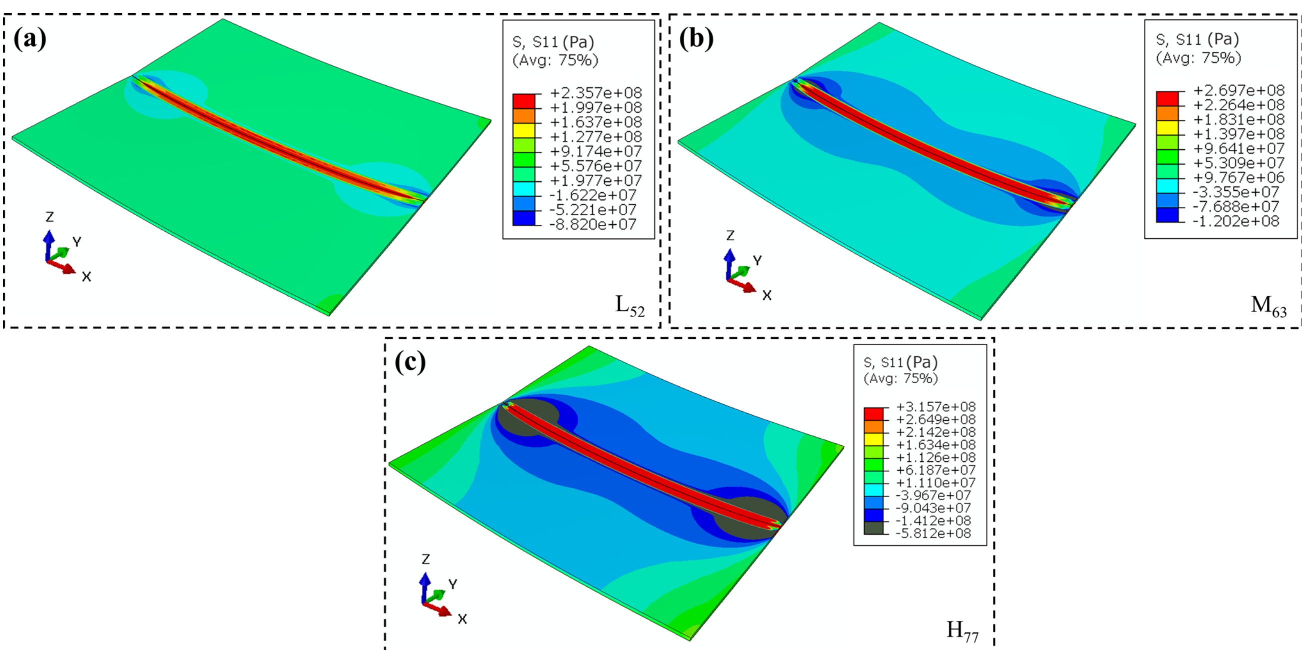

Fig. 16 Residual stress distribution along the longitudinal direction (S11) for different process conditions **a** L_{52}, **b** M_{63}, and **c** H_{77}

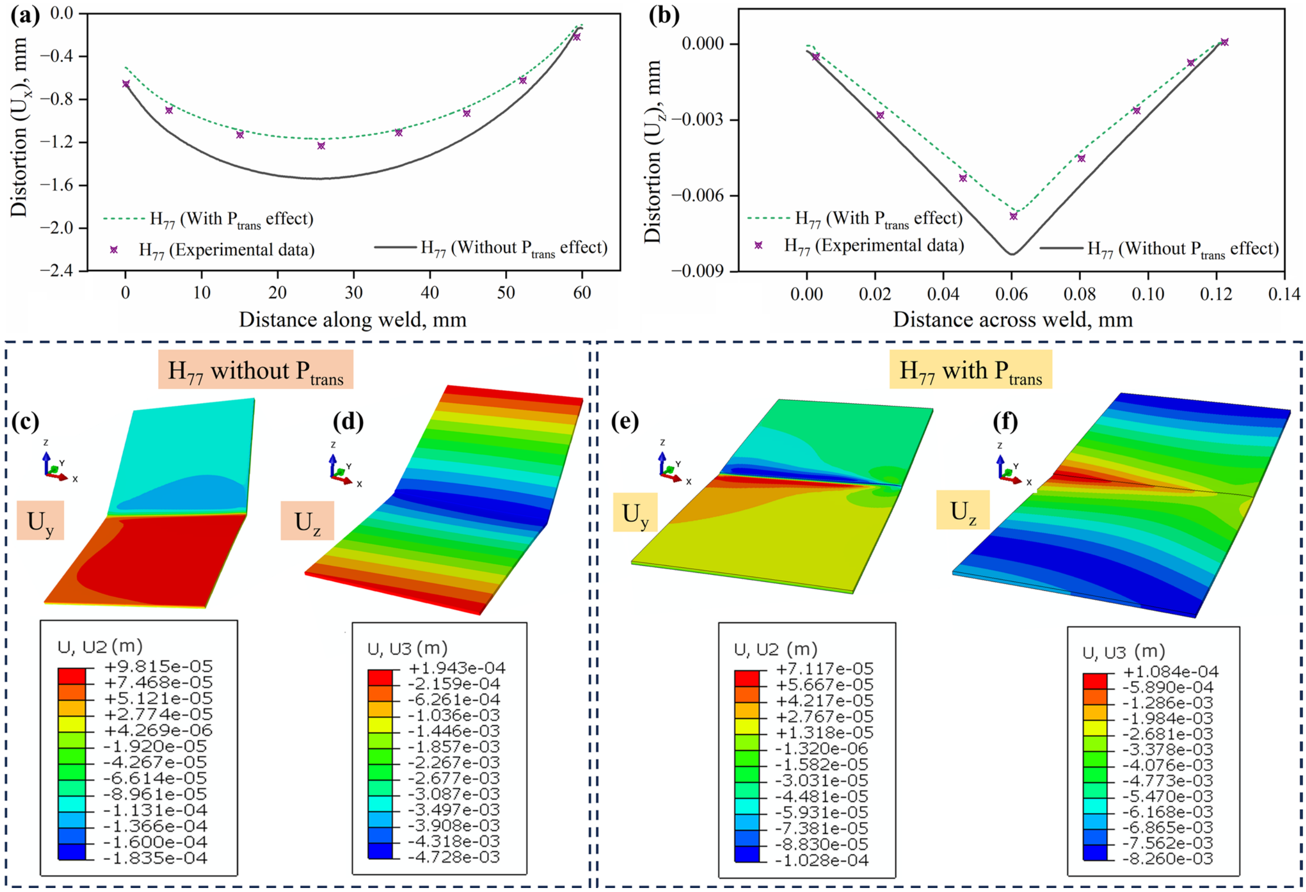

Fig. 17 **a** Distortion along the longitudinal direction (U_x), **b** out of the plane distortion (U_z); distortion contour for U_y and U_z **c**,**d** without phase transformation, and **e**,**f** with phase transformation for H_{77} process condition

measured as 1.17 and 1.54 mm, respectively. The experimental value determined from the CMM is 1.23 mm. Thus, the error in predicting U_x for the H_{77} process condition is evaluated as ~ 5% and ~ 25% with and without consideration of phase transformation, respectively. The significant error of U_x implies that the incorporation of phase transformation immensely aids in accurately predicting the value of distortion. Notably, the value of U_x is found to be highest for the H_{77} process condition. The probable reason for such a scenario is the involvement of a high amount of plastic strain induced in the joints. Figure 17b illustrates the out-of-the-plane distortion (U_z) for specimen H_{77}, wherein the maximum deflection occurs near the edges of the sheets, and the minimum deflection at the weld center. The maximum value of the deflection with and without phase transformation is identified as 0.008 and 0.00654 mm, respectively. The experimental data is measured as 0.0068 mm, and the corresponding error in predicting the value of U_z is evaluated as ~ 4% and ~ 17% with and without phase transformation, respectively. Similar to U_x, it is observed that the value of U_z is found to be highest for the high heat input process condition (H_{77}). Figure 17c-f represents the comparison between the transverse deflection (U_y) and out-of-plane distortion (U_z) distortion contour of the H_{77} sample. It is observed that the magnitude of U_y is maximum without consideration of the phase transformation effect, and the value of U_y is lowered with consideration of the phase transformation effect. The out-of-the-plane distortion is shown in Fig. 17d,f, where the deflection is the highest at the edges, and reduces with consideration of the phase transformation effect. The incorporation of phase transformation prevents overestimation of stress value due to consideration of compressive stresses created by $\delta_{ferrite}$ enriched core. Similarly, a reduction in deflection value is observed due to partial cancelation of deflection in U_x and U_z directions. A similar trend is reported in the martensitic transformation of medium carbon steel, resulting in a considerable reduction in distortion with the incorporation of the phase transformation effect [27].

The microstructural features, residual stress, distortion, and temperature variation in dissimilar welding of steels using μ-PAW are discussed in this section. The summary of the comparative results between experiments and numerical calculation is presented in Table 4. The complete details of the quantitative results of the input

Table 4 A summary of the comparative results between numerical and experimental measurements

Heat input (J/mm		52 (L_{52})			63 (M_{63})		77 (H_{77})	
Cooling rate (K/s)		1063			832		583	
$Cr_{eq.}/Ni_{eq.}$ ratio		1.77			1.65		1.54	
Lath size (nm)		412			723		1040	
PDAS (μm)		~10			~15		~20	
EBSD analysis		LAGBs⟶	23.64%		38.16%		48.99%	
		HAGBs⟶	76.36%		61.48%		51.01%	
Weld size (mm)	W_{opt}	Exp. ⟶	1.70	0.47	1.84	0.83	2.03	1.11
	W_{root}	Num. ⟶	1.67	0.43	1.86	0.78	1.98	1.03
Error ⟶			~1.77%	~8.51%	~1.08%	~6.02%	~2.46%	~7.21%
Peak temperature (K)			SS316L	SS310	SS316L	SS310	SS316L	SS310
		Exp. ⟶	1118	1258	1169	1304	–	–
		Num. ⟶	1177	1323	1231	1401	1299	1495
Error ⟶			~5.28%	~5.17%	~5.31%	~7.43%	–	–
Retained		Exp. ⟶		11.2	9.7		7.9	
$\delta_{ferrite}$ (%)		Num. ⟶		13.1	11.2		8.8	
Error ⟶				~16%	~15%		~11%	
Residual stress (S11, MPa)		Exp. ⟶		212	239		280	
		Num. ⟶		181	266		328	
Error ⟶				**~17%**	**~11%**		**~15%**	
Distortion (mm)					Without P_{trans} 77 J/mm (H_{77})		With P_{trans} 77 J/mm (H_{77})	
					U_x	U_z	U_x	U_z
		Exp. ⟶			1.23	0.0068	1.23	0.0068
		Num. ⟶			1.54	0.00654	1.17	0.008
Error ⟶					**~25%**	**~17%**	**~5%**	**~4%**

parameter (heat input) and the corresponding output results (cooling rate, peak temperature, $Cr_{eq.}/Ni_{eq.}$ ratio, lath size, PDAS, weld dimensions, retained $\delta_{ferrite}$ percentage, grain misorientation, longitudinal residual stress, and distortion) are presented here.

5 Conclusions

The current investigation is carried out to identify the influence of SSPT on residual stress developed for dissimilar joints formed by the μ-PAW welding process. Experimental and numerical analysis is carried out to predict mainly the retained $\delta_{ferrite}$ and residual stress generated in the dissimilar joints. The conclusive statements derived from the present work are as follows.

- The evaluated $Cr_{eq.}/Ni_{eq.}$ ratio ranges from 1.54 to 1.77, which suggests FA mode of solidification exists, where the FZ consists of $\delta_{ferrite}$ (skeletal and lathy) within the austenitic matrix.
- The retained $\delta_{ferrite}$ decreases (11.2 ⟶ 9.7 ⟶ 7.9%) with an increase in heat input (52 ⟶ 63 ⟶ 77 J/mm). The predicted values of $\delta_{ferrite}$ show a maximum error of ~16%. Further, a reduction in the peak intensity obtained from the XRD pattern confirms a decrease in $\delta_{ferrite}$ amount, when the heat input enhances.
- An increase in heat input is analogous to the reduction in cooling rate (1063 ⟶ 832 ⟶ 583 K/s) that allows the growth of $\delta_{ferrite}$ lath (412 ⟶ 723 ⟶ 1040 nm) and enhances the inter-dendritic gap (10 ⟶ 15 ⟶ 20 μm).
- The difference in the magnitude of the thermal expansion coefficient ($\alpha_{Ni} \sim 1.6\alpha_{Cr}$) corresponds to tensile residual stress in the γ-region (where Ni % is high) and compressive stress in the dendritic core (where Cr % is high). A low heat input condition (52 J/mm, highest retained $\delta_{ferrite}$) generates comparatively more compressive stress than high heat input conditions (63 and 77 J/mm).
- The deflection in the resulting dissimilar joints shows significant error (U_x ~25% and U_z ~17%) without consideration of the phase transformation effect and it is only U_x ~5% and U_z ~4% including the effect of the SSPT effect.

It is summarized that a successful joining of dissimilar materials can be achieved by using a minimum amount of heat input analogous to high $\delta_{ferrite}$ content, relatively finer lath size, and minimum gap between dendritic arms. The combination of such characteristics of $\delta_{ferrite}$ aids in reducing the residual stress generated.

Acknowledgements The authors gratefully acknowledge the NECBH and DBT (IIT Guwahati), Govt. of India, for the project no. BT/COE/34/SP28408/2018 for the FESEM instrumentation facility.

References

1. Banik SD, Kumar S, Singh PK, Bhattacharya S, Mahapatra MM. Distortion and residual stresses in thick plate weld joint of austenitic stainless steel: experiments and analysis. J Mater Process Technol. 2021;289:116944.
2. Ma C, Peng Q, Mei J, Han E-H, Ke W. Microstructure and corrosion behavior of the heat affected zone of a stainless steel 308L–316L weld joint. J Mater Sci Technol. 2018;34:1823–34.
3. Durgaprasad K, Pal S, Das M. Influence of cusp magnetic field on the evolution of metallurgical and mechanical properties in GTAW of SS 304. Int J Adv Manuf Technol. 2023;126:1–16.
4. Lin Y-C, Chou CP. A new technique for reducing the residual stress induced by welding in type 304 stainless steel. J Mater Process Technol. 1995;48:693–8.
5. Haldar V, Pal S. Influence of fusion zone metallurgy on the mechanical behavior of Ni-Based superalloy and austenitic stainless steel dissimilar joint. J Mater Eng Perform. 2023. https://doi.org/10.1007/s11665-023-08335-0.
6. Kumar, A., Bhattacharyya, A., Pandey, C.: Structural Integrity Assessment of Inconel 617/P92 Steel Dissimilar Welds Produced Using the Shielded Metal Arc Welding Process. J. Mater. Eng. Perform. (2023).
7. Anawa EM, Olabi A-G. Control of welding residual stress for dissimilar laser welded materials. J Mater Process Technol. 2008;204:22–33.
8. Kumar R, Mahapatra MM, Pradhan AK, Giri A, Pandey C. Experimental and numerical study on the distribution of temperature field and residual stress in a multi-pass welded tube joint of Inconel 617 alloy. Int J Press Vessels Pip. 2023;206:105034.
9. Kumar A, Guguloth K, Pandey SM, Fydrych D, Sirohi S, Pandey C. Study on microstructure-property relationship of inconel 617 Alloy/304L SS steel dissimilar welds joint. Metall Mater Trans A. 2023;54:3844–70.
10. Dawes, C.T.: Laser welding: a practical guide. Woodhead Publishing (1992)
11. Kumar B, Nagamani Jaya B. Thermal stability and residual stresses in additively manufactured single and multi-material systems. Metall Mater Trans A. 2023;54:1808–24.
12. Akbari D, Sattari-Far I. Effect of the welding heat input on residual stresses in butt-welds of dissimilar pipe joints. Int J Press Vessels Pip. 2009;86:769–76.
13. Maurya AK, Chhibber R, Pandey C. Studies on residual stresses and structural integrity of the dissimilar gas tungsten arc welded joint of sDSS 2507/Inconel 625 for marine application. J Mater Sci. 2023;58:8597–634.
14. Hsieh C-C. Microstructural evolution and examination of α'-martensite during a multi-pass dissimilar stainless steel GTAW process. Met Mater Int. 2008;14:643–8.
15. Hsieh C-C, Wu W. Phase transformation of δ→σ in multipass heat-affected and fusion zones of dissimilar stainless steels. Met Mater Int. 2011;17:375–81.
16. Kianersi D, Mostafaei A, Amadeh AA. Resistance spot welding joints of AISI 316L austenitic stainless steel sheets: phase transformations, mechanical properties and microstructure characterizations. Mater Des. 2014;61:251–63.
17. Harjo S, Tomota Y, Ono M. Measurements of thermal residual elastic strains in ferrite–austenite Fe–Cr–Ni alloys by neutron and X-ray diffractions. Acta Mater. 1998;47:353–62.
18. Thibault D, Bocher P, Thomas M, Gharghouri M, Côté M. Residual stress characterization in low transformation temperature 13% Cr–4% Ni stainless steel weld by neutron diffraction and the contour method. Mater Sci Eng A. 2010;527:6205–10.
19. Hsieh CC, Wang PS, Wang JS, Wu W. Evolution of microstructure and residual stress under various vibration modes in 304 stainless steel welds. Sci World J. 2014;2014:1–9.
20. Chen L, Mi G, Zhang X, Wang C. Numerical and experimental investigation on microstructure and residual stress of multi-pass hybrid laser-arc welded 316L steel. Mater Des. 2019;168:107653.
21. De A, DebRoy T. A perspective on residual stresses in welding. Sci Technol Weld Join. 2011;16:204–8.
22. Kesavan Nair P, Vasudevan R. Residual stresses of types II and III and their estimation. Sadhana. 1995;20:39–52.
23. Olabi, A.G., Hashmi, M.S.J.: Review of methods for measuring residual stresses in components. In: Proceedings of 9th Conf. on Manufacturing Research Sep (1993)
24. Deng D, Murakawa H. Influence of transformation induced plasticity on simulated results of welding residual stress in low temperature transformation steel. Comput Mater Sci. 2013;78:55–62.
25. Feng Z. Processes and mechanisms of welding residual stress and distortion. Woodhead Publishing: Elsevier; 2005.
26. Lindgren L-E. Numerical modelling of welding. Comput Methods Appl Mech Eng. 2006;195:6710–36.
27. Deng D. FEM prediction of welding residual stress and distortion in carbon steel considering phase transformation effects. Mater Des. 2009;30:359–66.
28. Zubairuddin M, Albert SK, Chaudhari V, Suri VK. Influence of phase transformation on thermo-mechanical analysis of modified 9Cr-1Mo steel. Procedia Mater Sci. 2014;5:832–40.
29. Hamelin CJ, Muránsky O, Smith MC, Holden TM, Luzin V, Bendeich PJ, Edwards L. Validation of a numerical model used to predict phase distribution and residual stress in ferritic steel weldments. Acta Mater. 2014;75:1–19.
30. Yaghi AH, Hyde TH, Becker AA, Sun W. Finite element simulation of welding and residual stresses in a P91 steel pipe incorporating solid-state phase transformation and post-weld heat treatment. J Strain Anal Eng Des. 2008;43:275–93.
31. Li S, Hu L, Dai P, Bi T, Deng D. Influence of the groove shape on welding residual stresses in P92/SUS304 dissimilar metal butt-welded joints. J Manuf Process. 2021;66:376–86.
32. Kumar B, Bag S. Phase transformation effect in distortion and residual stress of thin-sheet laser welded Ti-alloy. Opt Lasers Eng. 2019;122:209–24.
33. Kumar B, Bag S, Mahadevan S, Paul CP, Das CR, Bindra KS. On the interaction of microstructural morphology with residual stress in fiber laser welding of austenitic stainless steel. CIRP J Manuf Sci Technol. 2021;33:158–75.
34. Taraphdar PK, Kumar R, Pandey C, Mahapatra MM. Significance of finite element models and solid-state phase transformation on the evaluation of weld induced residual stresseS. Met Mater Int. 2021;27:3478–92.
35. Kubiak M, Piekarska W. Comprehensive model of thermal phenomena and phase transformations in laser welding process. Comput Struct. 2016;172:29–39.
36. Mi G, Xiong L, Wang C, Hu X, Wei Y. A thermal-metallurgical-mechanical model for laser welding Q235 steel. J Mater Process Technol. 2016;238:39–48.

37. Ghafouri M, Ahn J, Mourujärvi J, Björk T, Larkiola J. Finite element simulation of welding distortions in ultra-high strength steel S960 MC including comprehensive thermal and solid-state phase transformation models. Eng Struct. 2020;219:110804.
38. Shen L, He Y, Liu D, Gong Q, Zhang B, Lei J. A novel method for determining surface residual stress components and their directions in spherical indentation. J Mater Res. 2015;30:1078–89.
39. Taraphdar PK, Thakare JG, Pandey C, Mahapatra MM. Novel residual stress measurement technique to evaluate through thickness residual stress fields. Mater Lett. 2020;277:128347.
40. Elata D, Abu-Salih S. Analysis of a novel method for measuring residual stress in micro-systems. J Micromechanics Microengineering. 2005;15:921.
41. Taraphdar PK, Kumar R, Giri A, Pandey C, Mahapatra MM, Sridhar K. Residual stress distribution in thick double-V butt welds with varying groove configuration, restraints and mechanical tensioning. J Manuf Process. 2021;68:1405–17.
42. Taraphdar PK, Mahapatra MM, Pradhan AK, Singh PK, Sharma K, Kumar S. Effects of groove configuration and buttering layer on the through-thickness residual stress distribution in dissimilar welds. Int J Press Vessels Pip. 2021;192:104392.
43. Nowacki J, Sajek A, Matkowski P. The influence of welding heat input on the microstructure of joints of S1100QL steel in one-pass welding. Arch Civ Mech Eng. 2016;16:777–83.
44. Pandey C, Mahapatra MM, Kumar P. A comparative study of transverse shrinkage stresses and residual stresses in P91 welded pipe including plasticity error. Arch Civ Mech Eng. 2018;18:1000–11.
45. Saha D, Pal S. Study on the microstructural variation and fatigue performance of microplasma arc welded thin 316L sheet. Proc. Inst. Mech Eng Part J Mater Des Appl. 2022;236:880–90.
46. Dwibedi S, Bag S. Development of micro-plasma arc welding system for different thickness dissimilar austenitic stainless steels. J Inst Eng India Ser C. 2021;102:657–71.
47. Mousavi SA, Miresmaeili R. Experimental and numerical analyses of residual stress distributions in TIG welding process for 304L stainless steel. J Mater Process Technol. 2008;208:383–94.
48. Kohli D, Rakesh R, Sinha VP, Prasad GJ, Samajdar I. Fabrication of simulated plate fuel elements: defining role of stress relief annealing. J Nucl Mater. 2014;447:150–9.
49. Dwibedi S, Bag S. Influence of process parameters on microstructural evolution, solidification mode and impact strength in joining of stainless steel thin sheets. Adv Mater Process Technol. 2021;8(sup3):1089–104.
50. Lippold, J.C., Kotecki, D.J.: Welding metallurgy and weldability of stainless steels. (2005)
51. Avrami M. Transformation-time relations for random distribution of nuclei kinetics of phase change II. J Chem Phys. 1940;8:212.
52. Feujofack Kemda BV, Barka N, Jahazi M, Osmani D. Modeling of phase transformation kinetics in resistance spot welding and investigation of effect of post weld heat treatment on weld microstructure. Met Mater Int. 2021;27:1205–23.
53. Kumar B, Bag S, Paul CP, Das CR, Ravikumar R, Bindra KS. Influence of the mode of laser welding parameters on microstructural morphology in thin sheet Ti6Al4V alloy. Opt Laser Technol. 2020;131:106456.
54. Ahn J, He E, Chen L, Wimpory RC, Dear JP, Davies CM. Prediction and measurement of residual stresses and distortions in fibre laser welded Ti-6Al-4V considering phase transformation. Mater Des. 2017;115:441–57.
55. Li Z, Feng G, Deng D, Luo Y. Investigating welding distortion of thin-plate stiffened panel steel structures by means of thermal elastic plastic finite element method. J Mater Eng Perform. 2021;30:3677–90.
56. Sun J, Liu X, Tong Y, Deng D. A comparative study on welding temperature fields, residual stress distributions and deformations induced by laser beam welding and CO2 gas arc welding. Mater Des. 2014;63:519–30.
57. Onink M, Brakman CM, Tichelaar FD, Mittemeijer EJ, Van der Zwaag S, Root JH, Konyer NB. The lattice parameters of austenite and ferrite in Fe-C alloys as functions of carbon concentration and temperature. Scr Metall Mater States. 1993;29:1011.
58. Saida K, Nishijima Y, Ogiwara H, Nishimoto K. Prediction of solidification cracking in laser welds of type 310 stainless steels. Weld Int. 2015;29:577–86.
59. Rong Y, Huang Y, Xu J, Zheng H, Zhang G. Numerical simulation and experiment analysis of angular distortion and residual stress in hybrid laser-magnetic welding. J Mater Process Technol. 2017;245:270–7.
60. Standard, A.: E230/E230M- 12. Stand. Specif. Temp.-Electromotive Force Emf Tables Stand. Thermocouples ASTM Int. West Conshohocken Pa. (2012)
61. Lee Y, Nordin M, Babu SS, Farson DF. Effect of fluid convection on dendrite arm spacing in laser deposition. Metall Mater Trans B. 2014;45:1520–9.
62. Ragavendran M, Vasudevan M. Laser and hybrid laser welding of type 316L (N) austenitic stainless steel plates. Mater Manuf Processes. 2020;35:922–34.
63. Kumar S, Shahi AS. Effect of heat input on the microstructure and mechanical properties of gas tungsten arc welded AISI 304 stainless steel joints. Mater Des. 2011;32:3617–23.
64. Yan S, Shi Y, Liu J, Ni C. Effect of laser mode on microstructure and corrosion resistance of 316L stainless steel weld joint. Opt Laser Technol. 2019;113:428–36.
65. Astm: Standard Test Method for Determining Volume Fraction by Systematic Manual Point Count. Practice. 1–7 (2011)
66. Bansal A, Sharma AK, Das S, Kumar P. On microstructure and strength properties of microwave welded Inconel 718/stainless steel (SS-316L). Proc. Inst. Mech Eng Part J Mater Des Appl. 2016;230:939–48.
67. Saranarayanan R, Lakshminarayanan AK, Venkatraman B. A combined full-field imaging and metallography approach to assess the local properties of gas tungsten arc welded copper—stainless steel joints. Arch Civ Mech Eng. 2019;19:251–67.
68. Jiang Z, Tao W, Yu K, Tan C, Chen Y, Li L, Li Z. Comparative study on fiber laser welding of GH3535 superalloy in continuous and pulsed waves. Mater Des. 2016;110:728–39.
69. Jiang Z, Chen X, Li H, Lei Z, Chen Y, Wu S, Wang Y. Grain refinement and laser energy distribution during laser oscillating welding of Invar alloy. Mater Des. 2020;186:108195.
70. Zhang H, Xu M, Liu Z, Li C, Kumar P, Liu Z, Zhang Y. Microstructure, surface quality, residual stress, fatigue behavior and damage mechanisms of selective laser melted 304L stainless steel considering building direction. Addit Manuf. 2021;46:102147.
71. Zhang H, Xu M, Kumar P, Li C, Dai W, Liu Z, Li Z, Zhang Y. Enhancement of fatigue resistance of additively manufactured 304L SS by unique heterogeneous microstructure. Virtual Phys Prototyp. 2021;16:125–45.
72. Baruah M, Bag S. Influence of pulsation in thermo-mechanical analysis on laser micro-welding of Ti6Al4V alloy. Opt Laser Technol. 2017;90:40–51.
73. Ishigami A, Roy MJ, Walsh JN, Withers PJ. The effect of the weld fusion zone shape on residual stress in submerged arc welding. Int J Adv Manuf Technol. 2017;90:3451–64.
74. Karunaratne MSA, Kyaw S, Jones A, Morrell R, Thomson RC. Modelling the coefficient of thermal expansion in Ni-based superalloys and bond coatings. J Mater Sci. 2016;51:4213–26.
75. Hosseini HS, Shamanian M, Kermanpur A. Characterization of microstructures and mechanical properties of Inconel 617/310 stainless steel dissimilar welds. Mater Charact. 2011;62:425–31.

76. Kumar C, Das M. Exploration of parametric effect on fiber laser weldments of SS-316L by response surface method. J Mater Eng Perform. 2021;30:4583–603.